

**REPORT DOCUMENTATION PAGE**

*Form Approved  
OMB No. 0704-0188*

The public reporting burden for this collection of information is estimated to average 1 hour per response, including the time for reviewing instructions, searching existing data sources, gathering and maintaining the data needed, and completing and reviewing the collection of information. Send comments regarding this burden estimate or any other aspect of this collection of information, including suggestions for reducing the burden, to the Department of Defense, Executive Services and Communications Directorate (0704-0188). Respondents should be aware that notwithstanding any other provision of law, no person shall be subject to any penalty for failing to comply with a collection of information if it does not display a currently valid OMB control number.

**PLEASE DO NOT RETURN YOUR FORM TO THE ABOVE ORGANIZATION.**

<b>1. REPORT DATE (DD-MM-YYYY)</b> 08-16-2011		<b>2. REPORT TYPE</b> Final		<b>3. DATES COVERED (From - To)</b> 05-15-2010 - 05-14-2011	
<b>4. TITLE AND SUBTITLE</b> Creating Extended and Dense Plasma Channels in Air by Using Spatially and Temporally Shaped Ultra-Intense Laser Pulses				<b>5a. CONTRACT NUMBER</b>	
				<b>5b. GRANT NUMBER</b> FA9550-10-1-0237	
				<b>5c. PROGRAM ELEMENT NUMBER</b>	
<b>6. AUTHOR(S)</b> Pavel Polynkin, Jerome Moloney				<b>5d. PROJECT NUMBER</b>	
				<b>5e. TASK NUMBER</b>	
				<b>5f. WORK UNIT NUMBER</b>	
<b>7. PERFORMING ORGANIZATION NAME(S) AND ADDRESS(ES)</b> College of Optical Sciences, University of Arizona 1630 E. University Blvd. Tucson, Arizona 85721				<b>8. PERFORMING ORGANIZATION REPORT NUMBER</b> 322930	
<b>9. SPONSORING/MONITORING AGENCY NAME(S) AND ADDRESS(ES)</b> Air Force Office of Scientific Research/RSE 875 North Randolph St. Arlington, VA 22203				<b>10. SPONSOR/MONITOR'S ACRONYM(S)</b> AFOSR	
				<b>11. SPONSOR/MONITOR'S REPORT NUMBER(S)</b> AFRL-OSR-VA-TR-2012-0782	
<b>12. DISTRIBUTION/AVAILABILITY STATEMENT</b> Distribution Statement A					
<b>13. SUPPLEMENTARY NOTES</b> Results summarized in this report are under review/to be published in peer-reviewed journals.					
<b>14. ABSTRACT</b> The experimental research under this program was supporting the on-going AFOSR MURI program on theoretical and numerical studies of femtosecond laser filamentation. The particular projects that we pursued in the course of this program are: 1. Creation of extended and dense plasma channels in air and other gases using a nanosecond-femtosecond dual-pulse laser excitation scheme. 2. Generation of regular arrays of plasma channels using femtosecond Bessel beams of higher order 3. Application of accelerating Airy temporal waveforms to ultrafast nonlinear optics 4. Generation of harmonics of tightly focused mid-IR pulses in ambient air.					
<b>15. SUBJECT TERMS</b> Nonlinear optics with ultrashort and ultraintense laser pulses, beam and pulse shaping, femtosecond laser filamentation					
<b>16. SECURITY CLASSIFICATION OF:</b>			<b>17. LIMITATION OF ABSTRACT</b> Unlimited	<b>18. NUMBER OF PAGES</b> 23	<b>19a. NAME OF RESPONSIBLE PERSON</b> Pavel Polynkin
<b>a. REPORT</b> Unclassified	<b>b. ABSTRACT</b> Unclassified	<b>c. THIS PAGE</b> Unclassified			<b>19b. TELEPHONE NUMBER (Include area code)</b> (520) 405-3767

Reset

## Final Performance Report for AFOSR grant #FA9550-10-1-0237

**PI:** Pavel Polynkin, College of Optical Sciences, University of Arizona  
**Program Manager:** Dr. Tatjana Curcic, AFOSR

**Summary:** Funds from this one-year grant supported one dedicated graduate student (Craig Ament) and the PI at 50%. The experimental research under this program was supporting the ongoing AFOSR MURI program on theoretical and numerical studies of femtosecond laser filamentation. The particular projects that we pursued in the course of this program are:

1. Creation of extended and dense plasma channels in air and other gases using a nanosecond-femtosecond dual-pulse laser excitation scheme.
2. Generation of regular arrays of plasma channels using femtosecond Bessel beams of higher order
3. Application of accelerating Airy temporal waveforms to ultrafast nonlinear optics
4. Generation of harmonics of tightly focused mid-IR pulses in ambient air.

The results of this work have been reported in six peer-reviewed publications, two of which appeared in press and four others are presently under review, as well as in four invited talks at international conferences and one post-deadline paper at CLEO in Baltimore, MD. The preprints of the papers under review are attached at the end of this report. Based on the results of his research, Craig Ament, the graduate student involved in the program, has been recently awarded the Directed Energy Professional Society (DEPS) graduate fellowship.

### List of publications acknowledging the support from this grant:

1. P. Polynkin, M. Kolesik, E. Wright, J. Moloney, "Experimental Tests of the New Paradigm for Laser Filamentation in Gases", *Phys. Rev. Lett.* vol. 106, p. 153902 (2011).
2. P. Hemmer, R. Miles, P. Polynkin, T. Siebert, A. Sokolov, P. Sprangle, M. Scully, "Standoff spectroscopy via remote generation of a backward-propagating laser beam", *Proc. Nat. Acad. Sci.* vol. 108, p. 3130 (2011).
3. P. Polynkin, J. Moloney, "Optical Breakdown of Air Triggered by Femtosecond Laser Filaments", *under review*.
4. S. Shiffler, P. Polynkin, J. Moloney, "Filamentation of ultra-intense higher-order Bessel beams in water", *under review*.
5. C. Ament, P. Polynkin, J. Moloney, "Supercontinuum Generation with Femtosecond Self-Healing Airy Pulses", *under review*.
6. G. Ariunbold, P. Polynkin, J. Moloney, "Third and fifth harmonic generation by tightly focused femtosecond pulses at 2.2  $\mu\text{m}$  wavelength in air", *under review*.

### List of presentation acknowledging the support from this grant:

1. C. Ament, P. Polynkin, J. Moloney, "Supercontinuum Generation with Self-Healing Airy Pulses", Conf. Lasers and Electro-Optics (CLEO), Baltimore, MD, May 1, 2011, Postdeadline paper PDPC9.
2. P. Polynkin, "Filamentation of beam and pulse shaped femtosecond laser pulses" (Invited), The 41<sup>st</sup> Winter Colloquium on Physics of Quantum Electronics, Snowbird, Utah, January 2-6, 2011.
3. P. Polynkin, S. Shiffler, C. Ament, M. Kolesik, E. Wright, J. Moloney, "Filamentation of Beam Shaped Femtosecond Laser Pulses in Gases and Liquids" (Invited), CLEO Europe, Munich, Germany, 22-26 May, 2011.
4. P. Polynkin, "Experimental program on ultrafast laser filamentation at the university of Arizona" (Invited), Ninth Ultrashort Pulse Laser Workshop (as part of the Advanced Higher Power Laser Review), Santa Fe, NM, 6-9 June 2011.

5. P. Polynkin, C. Ament, S. Shiffler, M. Kolesik, E. Wright, J. Moloney, "Experimental program on ultrafast laser filamentation at the University of Arizona" (Invited), 20<sup>th</sup> International Laser Physics Workshop LPHYS'11, Sarajevo, July 11-15, 2011.

In what follows, the results of the research under this program are briefly summarized. More details can be found in the preprints of submitted papers that are attached at the end of this report.

### 1. Generation of extended and dense plasma channels in air using igniter-heater excitation scheme

Femtosecond laser filamentation allows for a substantial degree of control over plasma generation in the ambient air. The longitudinal position of the plasma filament can be straightforwardly manipulated by introducing a negative temporal chirp onto the laser pulse. As the chirped pulse propagates in the dispersive air, it is gradually compressed in time domain, reaching its maximum peak power at a particular propagation distance determined by the value of the chirp. The placement of the plasma channels within the transverse beam profile can be controlled by beam shaping.

Longitudinally extended plasma channels generated in air through femtosecond laser filamentation have numerous potential applications such as the guidance of electricity and emission of THz radiation. However, the density of free electrons generated through femtosecond filamentation in air, under typical conditions, is only about  $10^{22} \text{ m}^{-3}$ , which is too low for many applications.

In this program, we have conducted preliminary experiments on the generation of dense plasma channels through the combined application of ultraintense femtosecond and high-energy nanosecond laser pulses. The laser hardware used in this research has been acquired under the support of two rounds of AFOSR DURIP program, and the theoretical support has been provided through the interaction with the AFOSR-supported MURI on laser filamentation.

The experimental setup used in this work is schematically shown in Figure 1. The optical breakdown of the ambient air is driven by 10 ns-long heater pulses generated by a Q-switched Nd:YAG laser operating at 1064 nm wavelength. The maximum pulse energy of the heater laser is 3.3 J. The heater pulses are combined with femtosecond igniter pulses at 800 nm wavelength. The igniter pulses are temporally chirped to about 500 fs duration in order to avoid filamentation and associated damage in the dichroic beam combiner. The heater beam is focused by an axicon lens with the apex angle of  $175^\circ$ . The femtosecond igniter is weakly focused by an ordinary lens with the focal length of 0.5 m. Prior to the lens, the igniter beam is apertured in order to clear a hole made on the axis of the axicon lens used to focus the heater.

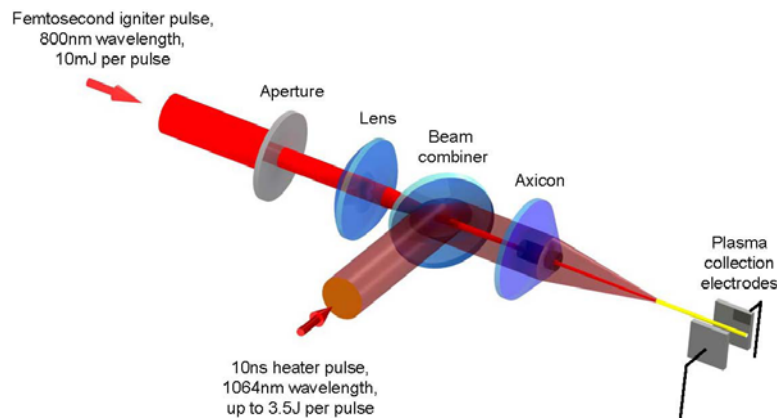


**Figure 1:** Schematic of the igniter-heater setup for dense plasma channel generation in air.

Using this setup, we have demonstrated that the density of the dilute plasma left in the wake of the femtosecond laser filament can be boosted by a factor of up to 200 by the application of the properly timed nanosecond pulse with Joule-level pulse energy. Quite naturally, the amount of the plasma-density enhancement depends on the delay between the two pulses. The enhancement shows clear threshold-like dependencies on the energies of both heater and igniter pulses.

This behavior is currently being modeled by the participants of the AFOSR-supported MURI on laser filamentation. The preliminary modeling results indicate that heating of the electron plasma by the heater pulse plays a major role in the development of the optical gas breakdown, as the electron temperature is directly related to the recombination rate of the plasma. We anticipate that the effect will be dramatically different in an atomic gas such as Argon. We have conducted preliminary experiments on the igniter-heater technique in Argon atmosphere and indeed observed a different breakdown regime from that in the air. This work is currently in progress. Our ultimate goal is to develop the igniter-heater approach into a viable technique for the controllable generation of dense plasma channels and channel arrays that would be suitable for such applications as guiding microwaves.

## 2. Filamentation of femtosecond Bessel beams of higher order

Early on in filamentation studies, it was realized that beam shaping offers an effective means of control over the extent of the generated filaments and their placement within the beam profile. The application of various beam shapes to filament formation, in both gaseous and condensed media, has been extensively studied in the past. Examples of beams previously used for the formation of filaments with particular properties include fundamental Bessel beams, vortex beams, necklace beams, and self-bending Airy beams.

We have conducted experiments on filamentation of femtosecond Bessel beams of higher order in water. In addition to being optical vortices, these beams are diffraction-resistant. They have bottle-like transverse intensity distributions that retain their shapes on propagation over extended distances. The goal of our study is to use these properties of higher-order Bessel beams for the generation of extended, bottle-like distributions of filaments that may be useful in applications.

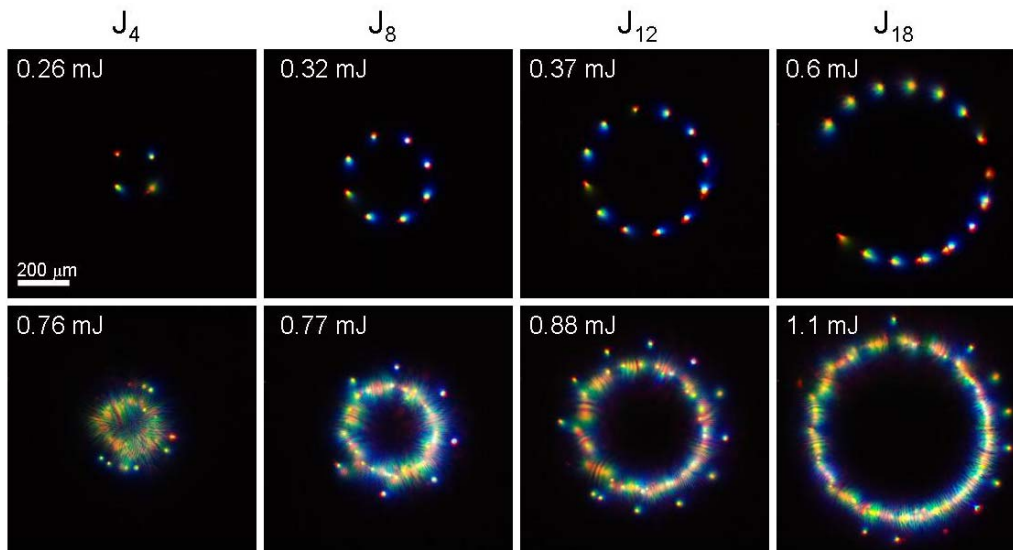


**Figure 2:** Filamentation of Bessel beams of various orders in water. The beams are generated from a fundamental Gaussian beam by a programmable phase mask.

Examples of the filament patterns formed by Bessel beams of various orders are shown in Figure 2. The self-focusing collapse is accompanied by the emission of the forward-propagating white-light continuum radiation.

If the dominant rings of the Bessel beams were perfectly smooth,  $2n+1$  filaments would be expected to form on the main ring of the  $n^{\text{th}}$ -order beam due to the azimuthal modulation instability. However, in our case, the placement of filaments is forced by the beaded structure of the beams, which is caused by the  $2\pi$ -modulo phase mask that we use to generate these beams. As the pulse energy is increased further, filaments start forming on the secondary rings of the beams, as shown in the bottom row of Figure 2.

Our experiments in water involved femtosecond Bessel beams with moderate energy  $\sim 1$  mJ. We are presently extending this work onto filamentation of much more energetic Bessel beams in air. To create higher-order Bessel beams with high energy, we use static phase masks fabricated for us by an affiliated holography group at the University of Arizona. The involvement of that group into this work was partially supported through this program which paid for materials and supplies as well as for the part-time support of the technician involved in the mask fabrication. The major challenge of the work on filamentation of higher-order Bessel beams in air is associated with the resistance of these beams to filamentation. The total energy of femtosecond laser pulses available to us is limited to about 35 mJ, and only few percent of that energy is carried by the center ring of a higher-order Bessel beam where the filaments are formed. This work is presently on-going.

### 3. Generation of sophisticated spatio-temporal pulse waveforms including various light bullets and application of these waveforms to filamentation studies.

In order to develop techniques for control over filament formation and dynamics, we have recently started experimenting with temporal shaping of femtosecond laser pulses. The particular pulse shape that we have studied in detail is the accelerating Airy pulse. Our initial experiments in this area focused on the generation of these pulses, their characterization, and application of these pulses to supercontinuum generation in optical fibers. This is a relatively simple one-dimensional problem, in which the transverse beam profile is invariant on propagation as it is defined by the properties of the optical fiber where laser pulses propagate.

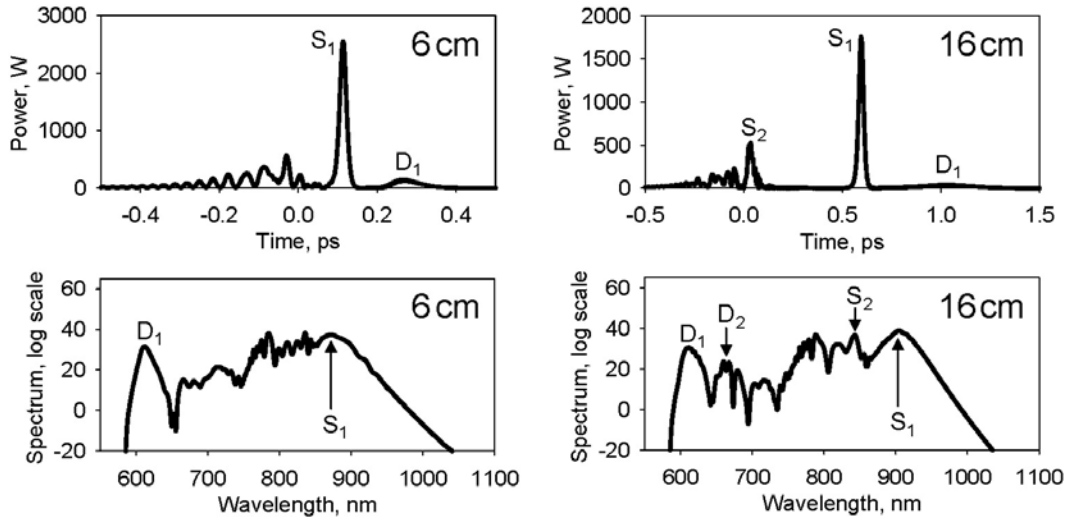


**Figure 3:** Top row, left: Temporal waveforms of the Airy pulse with  $-60,000 \text{ fs}^3$  cubic spectral phase after 6 cm propagation in the fiber. The main peak of the Airy waveform has produced a soliton-dispersive wave pair and is nearly regenerated. Right: Same after 16 cm propagation. The regenerated main peak of the pulse has produced another soliton-dispersive wave pair. Bottom row: Corresponding spectra.

We have conducted both numerical simulations and experiments on the propagation of Airy pulses in a highly-nonlinear optical fiber and found that the pulse propagation dynamic is different

for the cases when the tail of the Airy waveform propagates in front of and behind the main peak of the pulse. In the first case, the dominant peak of the pulse recreates itself after several soliton formation events, resulting in the generation of distinct dispersive-wave features in the output spectrum. In the second case, the soliton generated from the first collapse of the main peak of the pulse passes through the tail of the waveform and disrupts its ability to self-regenerate. The results of the modeling are in qualitative agreement with the experiments. The temporal dynamics and supercontinuum spectra generated by an Airy pulse propagating tail-first are shown in Figure 3.

We have recently extended this work on the studies of filamentation with self-healing Airy waveforms in water. The examples of the angularly-resolved spectra, for the cases of Airy pulses propagating tail-first and peak-first are shown in Figure 4. These patterns, in which the emission wavelength is resolved along the horizontal axis and the emission angle with respect to the geometrical beam axis is resolved along the vertical axis, are indicative of the complex temporal evolutions of these pulse waveforms on propagation in the water. Similar to the case of the supercontinuum generation with Airy pulses, the orientation of the tail of the pulse affects the generated spectral features. We are presently conducting extensive numerical simulations of this complex propagation regime.

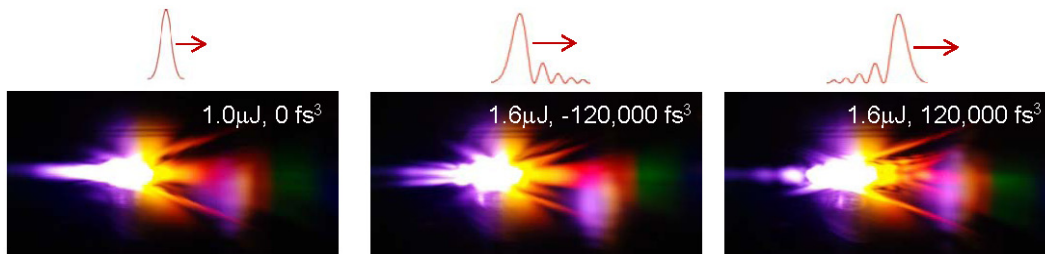


**Figure 4:** Angularly resolved spectra of the broadband forward-propagating emission from filaments generated by femtosecond temporal Airy pulses in water. The pulse energies and the values of the cubic phase are indicated in the individual figures. The case of a Gaussian pulse is shown in the left panel. This pattern is indicative of a single pulse-splitting event that accompanies filamentation in this case. In the case of an Airy pulse with the tail propagating first (center panel), there are two pulse-splitting events that result from the self-healing nature of the pulse waveform. In the case of the same waveform but with the tail propagating behind the main peak, the second splitting event is smeared out due to the interference between the splitting products and the tail of the waveform. This interference inhibits the pulse self-regenerating ability.

#### 4. Generation of harmonics of tightly focused mid-IR femtosecond pulses in ambient air.

This work targeted the implementation of the proposal put forth by the AFOSR-supported MURI team back in 2010. The goal was to validate or disprove the recently suggested high-order Kerr effect theory that claims that the conventional Kerr effect changes sign at high light intensities of the order of  $30 \text{ TW/cm}^2$ . If that suggestion is proven valid, then the generation of 3rd and 5th harmonic radiation that accompanies laser filamentation would become very efficient. Our results indicate that this is not the case, in agreement with the established paradigm of ultrafast nonlinear optics that is based on the conventional Kerr effect.

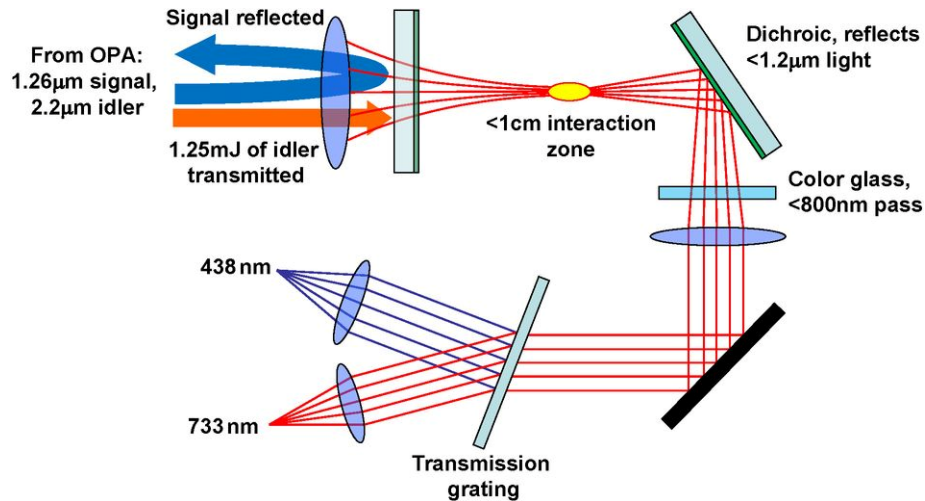


**Figure 5:** Experimental setup for 3<sup>rd</sup> and 5<sup>th</sup> harmonic generation in ambient air using mid-IR pulses at 2.2 $\mu\text{m}$  wavelength, in a tightly focused geometry.

Our experimental setup is schematically shown in Figure 5. Femtosecond pulses at 2.2  $\mu\text{m}$  center wavelength are produced by a commercial high-energy Optical Parametric Amplifier (OPA, Palitra-HE model by Quantronix Corporation). The OPA is pumped by about 40 fs-long, 20 mJ pulses at 800 nm wavelength generated by an ultrafast Ti:Sapphire amplifier chain operating at a 10 Hz pulse repetition frequency. The OPA is tuned to produce signal and idler pulses at 1.26  $\mu\text{m}$  and 2.20  $\mu\text{m}$  center wavelengths, respectively. The output beam from the OPA has a diameter of about 10 mm. Both signal and idler pulses have energies of about 1.5 mJ. The duration of the pulses is estimated by the OPA manufacturer at between 40 and 60 fs.

The third and fifth harmonics of the 2.2  $\mu\text{m}$  pump are generated in the ambient air, near the focal plane of the focusing lens. The estimated intensity of the pump beam near the focus is above the turnover point for the alleged sign reversal of the Kerr effect in the HOKE model and also above the ionization threshold of air. The length of the short and faint plasma spark generated in the vicinity of the interaction zone is less than 1 cm. Under these conditions, the ratio of the third and fifth harmonic yields, according to the high order Kerr effect theory, should approach one.

After collimation with another lens, the signals at third and fifth harmonics are spatially separated by a 300 lines per millimeter transmissive diffraction grating. The spectra of the two harmonics are recorded by a fiber-coupled spectrometer (model USB4000 by Ocean Optics Corporation), with the aid of two additional lenses that separately focus the harmonic beams after they are separated by the grating. These spectra are shown in Figure 6. They are centered at 733 nm and 438 nm, very close to one-third and one-fifth of the pump wavelength of 2.20  $\mu\text{m}$ .

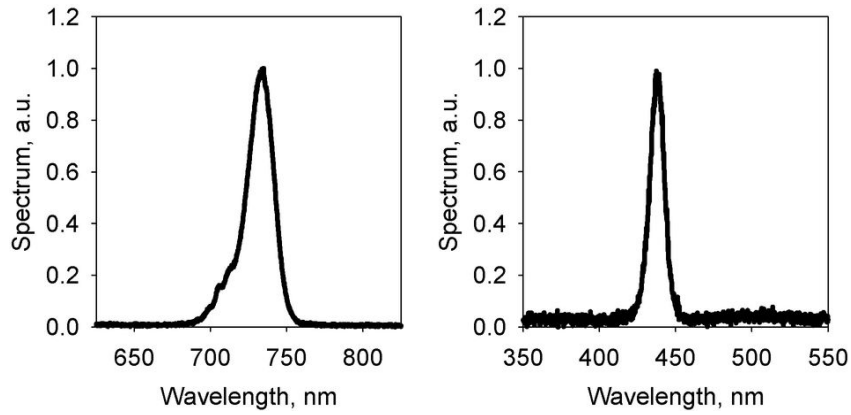


**Figure 6:** Measured spectra of the third and fifth harmonics.

The energies of the two harmonic pulses are measured by dedicated silicon detectors that were calibrated against a pyroelectric detector, using reference laser pulses at 800 nm wavelength. Accounting for all losses experienced by the generated harmonics in our setup, the energies of the third and fifth harmonics are found equal to 1.9  $\mu\text{J}$  and 0.4 nJ, respectively. These pulse energies correspond to yields of about  $1.5 \times 10^{-3}$  for third harmonic and  $3.0 \times 10^{-7}$  for fifth harmonic, with respect to the energy of the pump pulse at 2.2  $\mu\text{m}$  wavelength in the interaction zone. The ratio of yields for the two harmonics is about  $2 \times 10^{-4}$ , in contradiction with the higher-order Kerr effect theory.

# Optical Breakdown of Air Triggered by Femtosecond Laser Filaments

Pavel Polynkin\* and Jerome V. Moloney

*College of Optical Sciences, The University of Arizona, Tucson, Arizona 85721, USA*

(Dated: June 15, 2011)

We report experiments on the generation of dense plasma channels in ambient air using a dual laser pulse excitation scheme. In our approach, the dilute plasma produced through the filamentation of an ultraintense femtosecond laser pulse is densified via avalanche ionization driven by a co-propagating nanosecond pulse with multi-Joule-level pulse energy.

PACS numbers: 52.38.-r, 52.25.Jm, 42.65.Jx, 34.80.Gs

Experiments on gas breakdown by powerful optical pulses date back to the early days of lasers. Shortly after the demonstration of Q-switching of a solid-state laser in the early 1960's [1], a Q-switched ruby laser was used for the generation of plasma sparks in various noble gases [2]. Subsequent studies of laser breakdown in gases were primarily motivated by the potential use of this phenomenon in controlled nuclear fusion. (For a review of the subject see, for example, [3].)

The mechanisms responsible for gas breakdown by nanosecond laser pulses are well understood. During breakdown, free electrons are accelerated by the laser field through the inverse bremsstrahlung process which involves their collision with neutral and already ionized molecules. Once the accelerating electrons attain energy that equals the ionization potential of the neutral molecules, these electrons impact-ionize the molecules forming an electron avalanche. The few seed electrons needed to start the avalanche are typically provided by the multi-photon ionization of the easily ionizable impurities in the gas.

At a given pulse duration, optical breakdown by a nanosecond laser pulse is a threshold-like process with respect to the peak intensity of the pulse. The numerical value of this threshold depends on various parameters such as gas pressure and composition as well as on the focusing conditions. Furthermore, the threshold intensity can vary by as much as two orders of magnitude due to the presence of aerosols or dust in the gas [4]. For clean, dust-free air, the breakdown intensity threshold is of the order of  $10^{15}$  W/m<sup>2</sup>. Because of such a high optical intensity required for the initiation of the breakdown, breakdown experiments are typically conducted using tightly focused laser beams. The resulting dense plasma plumes, under typical atmospheric conditions, are less than one centimeter long.

In the last decade, a different mechanism of free-charge generation in gases, through femtosecond laser filamentation, has been extensively studied [5]–[7]. In a femtosecond laser filament, plasma generation via multi-photon ionization of the gas molecules constitutes the natural mechanism that balances the transverse collapse of the beam due to self-focusing.

Femtosecond laser filamentation allows for a substantial degree of control over plasma generation in the ambient air. The longitudinal position of the plasma fila-

ment can be straightforwardly manipulated by introducing a negative temporal chirp onto the laser pulse. As the chirped pulse propagates in the dispersive air, it is gradually compressed in time domain, reaching its maximum peak power at a particular propagation distance determined by the value of the chirp. The placement of the plasma channels within the transverse beam profile can be controlled by beam shaping [8].

Longitudinally extended plasma channels generated in air through femtosecond laser filamentation have numerous potential applications such as the guidance of electricity and emission of THz radiation. However, the density of free electrons generated through femtosecond filamentation in air, under typical conditions, is only about  $10^{22}$  m<sup>-3</sup> [9], which is too low for many applications.

In this Letter, we report experiments on the generation of dense plasma channels through the combined application of ultraintense femtosecond and high-energy nanosecond laser pulses. Following the terminology used in the laser particle acceleration community, we will refer to this approach as the “igniter-heater” scheme. In this approach, the femtosecond igniter pulse creates seed free electrons via multi-photon ionization. The co-propagating nanosecond heater pulse multiplies these seed electrons in an optically-driven avalanche. Our goal is to develop a viable technique for the controllable generation of extended and dense plasma channels and channel arrays in air, which are of interest in many applications.

The combined femtosecond-nanosecond excitation of plasma in gases has been previously used for the generation of short, dense plasma channels used in table-top particle acceleration [10] and in Raman amplification of laser light in plasma channels [11]. The experimental geometries used in those works resulted in the generation of, at most, several centimeter-long dense plasma channels and were not straightforwardly applicable for the generation of such channels at range.

In the context of filamentation science, experiments on dual-pulse femtosecond-nanosecond excitation have been also reported previously. However, the emphasis has been on heating, maintenance or revival of the dilute plasma in filaments, not on the substantial multiplication of the number of electrons in an avalanche-like process driven by the nanosecond pulse [12],[13]. In the above works, the femtosecond and nanosecond pulses in the two-pulse sequence were separated by a long time interval of up to

several milliseconds. In such a situation, the nanosecond pulse causes the liberation of the small amount of electrons that attach themselves to neutral oxygen molecules in the air filament. The femtosecond filament can be revived in this scenario, but plasma density in the revived filament typically remains low.

In the present work, plasma generation occurs in a different regime, in which the nanosecond heater pulse directly amplifies free electrons left in the wake of the femtosecond igniter pulse that undergoes filamentation. Accordingly, the two pulses in our case are temporally overlapping or nearly overlapping. As we will show, our approach results in a substantial boost of the plasma density relative to that in the femtosecond filament alone. The realization of our approach requires heater pulses with high pulse energies of the order of several Joules. This requirement may have been the reason why similar experiments have not been reported previously.

Let us make some basic estimates. Complete single-electron ionization of oxygen and nitrogen in the air filament will require certain energy that the nanosecond heater pulse will have to expend per unit length of the generated plasma channel. The ionization potentials of oxygen and nitrogen molecules are approximately 12 eV and 16 eV, and their fractional contents in the common air are 21% and 78%, respectively. The total particle density in the air is  $2.7 \times 10^{25} \text{ m}^{-3}$ . The diameter of a typical femtosecond laser filament in air is about  $100 \mu\text{m}$ . The ionization of all molecules in such a channel will require the expenditure of about 0.5 J of energy per meter of the channel. Contemporary commercial Q-switched Nd:YAG lasers are available with pulse energies of up to 50 J. Thus, from the energy standpoint, the generation of a completely ionized,  $100 \mu\text{m}$ -thick plasma channel or an array of several such channels, with the length of the order of tens of meters, is feasible.

To estimate the peak-power requirement for the heater pulse, we will follow [14] and assume that, in the laser-driven avalanche, the energy of a free electron in the laser field is increased by one ponderomotive energy on every collision with a neutral or already ionized molecule. Through the entire avalanche process, excluding few final electron generations, the densities of both electrons and ions remain low compared to the density of neutral molecules. Under these conditions, collisions between electrons and ions can be ignored as they are much less frequent compared to the electron collisions with neutral molecules.

The rate equation for the energy of a particular electron reads:

$$\frac{d\epsilon(t)}{dt} = \frac{e^2 I(t)}{2c\epsilon_0 m_e \omega_0^2} \cdot f_{em}(t), \quad (1)$$

where  $I(t)$  is the time-dependent intensity of the nanosecond heater pulse,  $e$  and  $m_e$  are electron charge and mass, respectively,  $c$  is the speed of light in free space,  $\epsilon_0$  is the dielectric constant of vacuum, and  $\omega_0$  is the optical frequency of the heater pulse.  $f_{em}$  is the frequency of collisions

between electrons and neutral molecules. It can be estimated as follows:

$$f_{em}(t) \approx \sigma_{em} \cdot N_m \cdot v_e(t) = \sigma_{em} \cdot N_m \cdot \sqrt{2\epsilon(t)/m_e}, \quad (2)$$

where  $\sigma_{em}$  is the collisional cross-section which is assumed to be independent of the electron energy.  $N_m$  is the density of molecules in the air, which remains approximately constant through the entire development of the avalanche, except for the last few generations.  $v_e(t)$  is the time-dependent speed of the electron.

With the exception of the seed electrons provided by the femtosecond filament, the energy evolution for each particular electron, irrespectively to which electron generation in the avalanche it belongs to, starts from a low value of the order of one ponderomotive energy and ends with the energy approximately equal to the ionization potential  $E$  of a neutral molecule. Equation (1) is straightforwardly integrated from 0 to  $\tau$ , which is the time interval required for an electron to gain energy equal to the ionization potential. (We assume, for simplicity, that all molecules in the air have approximately the same ionization potential.) The result can be written as follows:

$$\tau \approx \frac{2c\epsilon_0 m_e \omega_0^2}{e^2 \sigma_{em} N_m I_0} \cdot \sqrt{2m_e E}, \quad (3)$$

where  $I_0$  is the peak intensity of the nanosecond heater pulse, assumed to have a rectangular temporal profile, for simplicity.

Through the development of the avalanche, the total number of electrons  $N_e(t)$  approximately doubles with every new generation of electrons. The doubling period equals  $\tau$  given by the formula (3) above. Thus

$$N_e(t) = N_0 \cdot 2^{t/\tau}, \quad (4)$$

where  $N_0$  is the density of the seed electrons. At breakdown, all molecules in the air should be ionized after the passage of the heater pulse, i.e.  $N_e(T) \approx N_m$ , where  $T$  is the duration of the heater pulse. Combining this with equation (3), we find the breakdown threshold intensity of the heater pulse in the form:

$$I_{th} \approx \frac{2c\epsilon_0 m_e \omega_0^2 \sqrt{2m_e E}}{e^2 \sigma_{em} N_m T} \cdot \frac{\ln(N_m/N_0)}{\ln 2} \quad (5)$$

The ratio of logarithms in the above equation equals the approximate number of electron generations required to

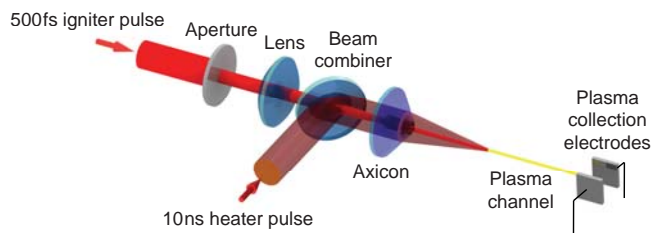


FIG. 1: Experimental setup used in the igniter-heater excitation scheme in air.

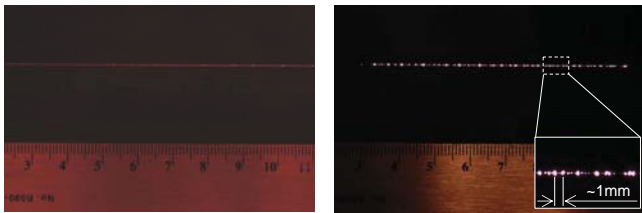


FIG. 2: Left: Photograph of a dilute plasma channel generated through filamentation of the femtosecond igniter pulse alone. To make the faint filament visible, the image is obtained by integration over 100 laser shots. Right: Single-shot image of a dense plasma channel generated through the joint application of the igniter and heater pulses. The inset shows the fragmentation of the channels into discrete plasma bubbles.

entirely ionize the air. For a spontaneous (unseeded) optical breakdown of common air, it is estimated that this number is about 40 [3], which corresponds to the seed electron density of the order of  $10^{13} \text{ m}^{-3}$ . Typical electron density in a femtosecond laser filament in the air is about  $10^{22} \text{ m}^{-3}$  [9]. If the avalanche is seeded by a filament, the number of electron generations required for the complete ionization will be about 11. Thus even though the dependence of the breakdown threshold intensity on the seed electron density is very weak (logarithmic), seeding by the filament will reduce the threshold breakdown intensity for the heater pulse by a factor of about 4, a substantial improvement relative to the unseeded breakdown.

For the experimental demonstration of our approach we use the setup shown schematically in Figure 1. The optical breakdown of ambient air is driven by 10 ns-long heater pulses generated by a Q-switched Nd:YAG laser operating at 1064 nm wavelength. The maximum pulse energy of the heater laser is 3.3 J. The heater pulses are combined with femtosecond igniter pulses at 800 nm

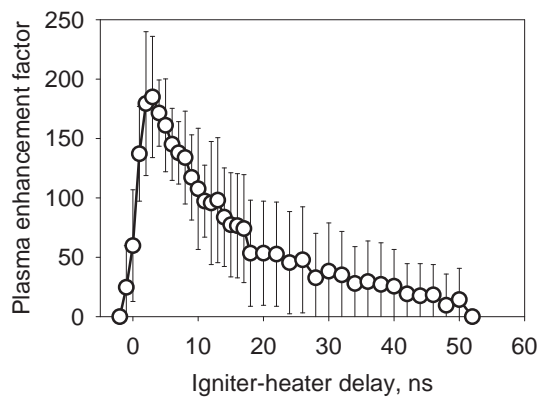


FIG. 3: Plasma-density enhancement factor relative to the density in the femtosecond igniter filament, vs. time delay between the igniter and heater pulses. Both pulses are at their maximum energies (15 mJ and 3.3 J for the igniter and heater pulses, respectively).

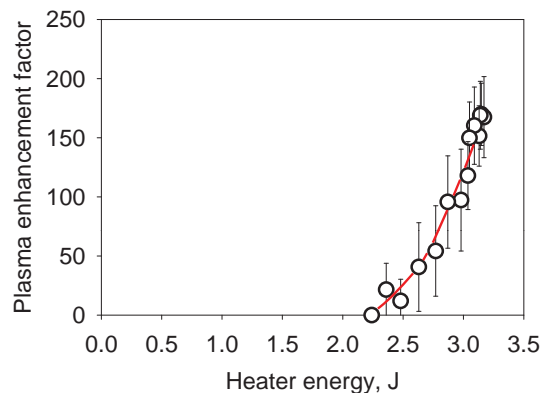


FIG. 4: Plasma-density enhancement factor as a function of the heater-pulse energy, at the optimum delay between the igniter and heater pulses.

wavelength. The igniter pulses are temporally chirped to about 500 fs duration in order to avoid filamentation and associated damage in the dichroic beam combiner. For the purposes that will be clear shortly, the heater beam is focused by an axicon lens with the apex angle of  $175^\circ$ . The femtosecond igniter is weakly focused by an ordinary lens with the focal length of 0.5 m. Prior to the lens, the igniter beam is apertured in order to clear a hole made on the axis of the axicon lens used to focus the heater. The maximum energy of the igniter pulse in the filamentation zone is about 15 mJ. Prior to focusing, the diameters of the incident heater beam and the apertured igniter beam are 20 mm and 5 mm, respectively. The pointing of the igniter beam is adjusted in order to overlap the femtosecond igniter filament with the  $\sim 30$  cm-long linear focal zone of the axicon. In our focusing geometry, the waist of the igniter pulse is approximately in the middle of the linear focus zone for the heater. Both igniter and heater lasers operate at 10 Hz pulse repetition frequency. The pulsed outputs from the two lasers are synchronized to better than 1 ns accuracy through a common triggering. The time delay between the pulses can be varied by means of an electronic delay unit placed in the trigger path for the heater laser.

With the heater beam turned off, the femtosecond igniter creates an  $\sim 20$  cm-long dilute filament, a photograph of which is shown in the left part of Figure 2. To make this faint filament visible, the photograph was integrated over about 100 laser shots. With both igniter and heater pulses applied at their maximum available energies and with the temporal delay between the pulses optimized, a seeded optical breakdown is observed reliably on every laser shot. The photograph of the breakdown region is shown in the right part of Figure 2. In this case, the plasma channel is bright and clearly visible on the single-shot image. The length of the densified plasma channel is about 10 cm. The channel is fragmented into multiple plasma bubbles separated by about 1 mm and positioned irregularly along the channel. This fragmentation is a result of the local plasma shielding for the

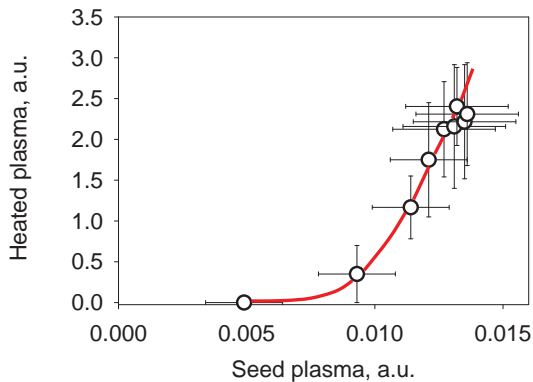


FIG. 5: Dependence of the plasma density generated through the joint application of the igniter and heater pulses, on the density of the seed plasma. Both seed and densified plasma densities are plot on the same arbitrary unit scale.

heater pulse. Using a heater beam in the form of the self-healing Bessel beam allows for the reconstruction of the main intensity peak on the beam axis after this peak is locally scattered by the dense plasma generated through the joint application of the igniter and heater pulses.

No breakdown is observed when the heater beam is applied at its maximum available energy but the igniter beam is turned off.

In order to quantify the density of the generated plasma, on a relative scale, we use a simple capacitive plasma probe described in detail elsewhere [15]. In this particular case, the probe has  $1\text{ cm} \times 1\text{ cm}$  collection electrodes that are separated by  $1.5\text{ cm}$ , charged to  $100\text{ V}$ , and placed approximately in the middle of the densified plasma channel.

Figure 3 shows the dependence of the plasma density generated through the joint application of the igniter and heater pulses, as a function of the delay between the pulses. Positive values of the delay correspond to the nanosecond heater pulse lagging behind the femtosecond igniter. Both pulses are at their maximum available energies. The plasma density is shown relative to the density with the heater pulse turned off (i.e. relative to the density of plasma in the seed filament). The maximum plasma-enhancement factor is about 200. For the delays

exceeding  $\sim 10\text{ ns}$ , the two pulses are no longer temporally overlapping, and the breakdown is seeded by the electrons left in the wake of the femtosecond pulse.

The dependence of the plasma density enhancement factor on the energy of the heater pulse is shown in Figure 4. The energy of the igniter pulse is kept at a maximum, and the temporal delay between the pulses is optimized to maximize the signal. A clear threshold with respect to the energy of the heater pulse is evident, as expected. The threshold heater energy of about  $2\text{ J}$  corresponds to the estimated peak on-axis intensity in the linear focus zone of the heater beam of about  $1.5 \times 10^{15}\text{ W/m}^2$ .

In Figure 5, we show the dependence of the generated electron density on the density of the seed electrons provided by the igniter filament. The density of the seed electrons was varied by changing the energy of the igniter pulse. The arbitrary units in both vertical and horizontal axes of this plot are the same. The threshold with respect to the density of the seed electrons is evident. The presence of this threshold appears to be counter-intuitive. It is not immediately obvious why the reduction of the density of seed electrons by, say, a factor of 2, completely halts the breakdown process. An adequate model utilizing kinetic equation formalism is necessary to understand this behavior.

In conclusion, we have conducted experiments on the generation of dense plasma channels in ambient air using the dual-pulse femtosecond-nanosecond excitation scheme. Reliable triggering of the optical breakdown by the femtosecond seed filament was demonstrated. A maximum plasma enhancement factor of about 200 in the dense plasma channel of about  $10\text{ cm}$  in length was measured. Further development of our approach and its scaling to higher energies of the heater pulse may yield a viable technique for the controllable generation of extended plasma channels and channel arrays in the atmosphere that can be useful in many applications.

The authors acknowledge helpful discussions with Ewan Wright. This work was supported by The United States Air Force Office of Scientific Research under programs FA9550-10-1-0237 and FA9550-10-1-0561.

\* Electronic address: [ppolynkin@optics.arizona.edu](mailto:ppolynkin@optics.arizona.edu)

- 
- [1] F. McClung, R. Hellwarth, *J. Appl. Phys.* **33**, 828 (1962).  
 [2] R. Meyerand, A. Haught, *Phys. Rev. Lett.* **11**, 401 (1963).  
 [3] *Principles of Laser Plasmas*, edited by G. Bekefi (Wiley, New York, 1976).  
 [4] D. Lencioni, *Appl. Phys. Lett.* **25**, 15 (1974).  
 [5] A. Couairon, A. Mysyrowicz, *Phys. Rep.* **441**, 47 (2007).  
 [6] L. Berge *et al.*, *Rep. Prog. Phys.* **70**, 1633 (2007).  
 [7] S. L. Chin, *Femtosecond Laser Filamentation* (Springer, 2010).  
 [8] G. Mechain, A. Couairon, M. Franco, B. Prade, A. Mysyrowicz, *Phys. Rev. Lett.* **93**, 035003 (2004).  
 [9] Y.-H. Chen, S. Varma, T. M. Antonsen, H. M. Milchberg, *Phys. Rev. Lett.* **105**, 215005 (2010).  
 [10] P. Volbeyn, E. Esarey, W. Lemans, *Phys. Plasmas* **6**, 2269 (1999).  
 [11] C.-H. Pai *et al.*, *Phys. Rev. Lett.* **101**, 065005 (2008).  
 [12] B. Zhou *et al.*, *Opt. Express* **17**, 11450 (2009).  
 [13] Z. Q. Hao *et al.*, *Appl. Phys. B* **80**, 627 (2005).  
 [14] J. Zeldovich, U. Raizer, *Sov. Phys. JETP* **20**, 772 (1965).  
 [15] P. Polynkin *et al.*, *Op. Express* **16**, 15733 (2008).

# Filamentation of ultra-intense higher-order Bessel beams in water

Stacy Shiffler<sup>1</sup>, Pavel Polynkin<sup>2,\*</sup>, Jerome Moloney<sup>2,3</sup>

<sup>1</sup> *Department of Physics, University of Arizona, Tucson, AZ 85721*

<sup>2</sup> *College of Optical Sciences, The University of Arizona, Tucson, Arizona 85721*

<sup>3</sup> *Department of Mathematics, University of Arizona, Tucson, AZ 85721*

\* *Corresponding author: ppolynkin@optics.arizona.edu*

Compiled August 7, 2011

We report experimental results on the self-focusing dynamics and filamentation of ultra-intense femtosecond Bessel beams of various orders in water. Regular filament patterns are formed on the bottle-like dominant intensity features of the beams. The peak-power thresholds for filamentation, at a particular distance, are relatively accurately estimated by the adaptation of the Marburger's formula derived earlier for Gaussian beams. The nonlinear conversion of the incident conical waves into the localized spatial wave packets propagating near the beam axis is observed. © 2011 Optical Society of America

*OCIS codes:* 190.5940, 190.7110, 050.4865

Ultrafast laser filamentation is an interdisciplinary field of modern physics that deals with the propagation of ultra-intense laser pulses in transparent dielectrics [1]-[3]. Most of the practical applications of filamentation are based on the properties of laser filaments in gases. However, transparent condensed media offer a convenient platform for experimental studies of filamentation and related phenomena, because the power threshold for self-focusing in this case is three orders of magnitude lower than that in gases.

Early on in filamentation studies, it was realized that beam shaping offers an effective means of control over the extent of the generated filaments and their placement within the beam profile. The application of various beam shapes to filament formation, in both gaseous and condensed media, has been extensively studied in the past. Examples of beams previously used for the formation of filaments with particular properties include fundamental Bessel beams [4, 5], vortex beams [6, 7], necklace beams [8], and self-bending Airy beams [9, 10].

In this Letter, we report experiments on filamentation of femtosecond Bessel beams of higher order in water. In addition to being optical vortices, these beams are diffraction-resistant. They have bottle-like transverse intensity distributions that retain their shapes on propagation over extended distances. The goal of our study is to use these properties of higher-order Bessel beams for the generation of extended, bottle-like distributions of filaments that may be useful in applications.

Ideal higher-order Bessel beams have their transverse amplitudes proportional to  $J_n(2\pi r/r_0)\exp(in\theta)$ , where  $J_n$  is the  $n^{\text{th}}$ -order Bessel function of the first kind,  $n$  is the beam order,  $(r, \theta)$  are transverse polar coordinates, and  $r_0$  is a scale factor. These beams are generated from an input plane wave through the phase-only beam amplitude modulation with the following transmission function [11]:

$$T_n(r, \theta) = \exp(in\theta) \exp\left(-\frac{2\pi ir}{r_0}\right). \quad (1)$$

Ideal higher-order Bessel beams have infinite energy flux and therefore they cannot be experimentally realized. The truncated versions of these beams are obtained by the application of the above spatial amplitude modulation to a finite-sized beam such as a Gaussian beam. The finite-energy Bessel beams retain the dispersion-resistance property of the ideal Bessel beams, but only for a limited propagation distance called the linear focal zone. The extent of this zone depends on the input beam parameters. Throughout this Letter, we will refer to the finite-energy Bessel beams as Bessel beams, although calling them Bessel-Gauss beams may be more appropriate. Examples of numerically simulated intensity profiles for selected higher-order Bessel beams are shown in Figure 1. Generally, Bessel beams with an order of one or larger have zero on-axis intensity. The diameter of their dominant intensity ring increases with the beam order.

The experimental setup used for the studies of filamentation of higher-order Bessel beams in water is schematically shown in Figure 2. The input Gaussian beam with 18 mm beam diameter is generated by a commercial ultrafast Ti:Sapphire-based amplifier that operates at 10 Hz pulse repetition frequency and outputs 40 fs-long pulses with a center wavelength of 800 nm. The input beam is transformed into Bessel beams of various orders through the spatial amplitude modulation in the form (1) imposed by a computer-controlled, reflective Spatial

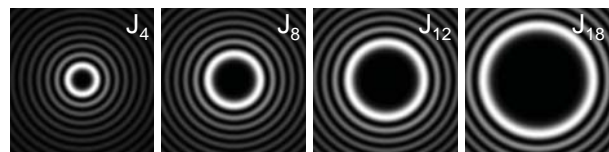


Fig. 1. Transverse intensity distributions for selected higher-order Bessel beams plotted on the same transverse scale.

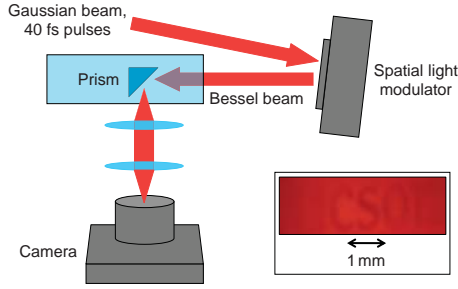


Fig. 2. Schematic of the experimental setup. The inset shows the word “Tucson” that was printed on the surface of the prism and imaged onto the camera. From this image, the imaging depth is estimated at about 1 mm.

Light Modulator (SLM, model X10468 by Hamamatsu Photonics). The SLM matrix has  $600 \times 800$  pixels and its clear aperture is 12 mm by 16 mm, thus it slightly clips the incident beam in both horizontal and vertical dimensions. The SLM did not show any signs of damage through the continuous exposure to the incident laser beam at the highest pulse energy level of 3 mJ.

The self-focusing and filamentation of the Bessel beams takes place in a glass-walled cuvette filled with distilled water. The size of the cuvette is  $1.6 \text{ mm} \times 2.0 \text{ mm} \times 7.6 \text{ mm}$ , and its length is chosen to be approximately equal to the dispersion length of the laser pulses in water. The distance between the entrance window of the cuvette and the SLM is 16 cm. For the particular realizations of higher-order Bessel beams that we use, the entire length of the cuvette is well within the linear focal zone of the beams.

To image the transverse intensity distribution of the beam propagating in the water, we immerse a small glass prism into the beam path. The uncoated glass surface of the prism reflects about 1.3% of the incident s-polarized beam. The reflected light is imaged onto a digital camera and photographed. For the imaging to be linear, it is important that the reflection off the prism surface is sufficiently small. The prism is translated along the beam path which allows to visualize the beam evolution on propagation through the water.

In Figure 3, we show the transverse intensity patterns imaged at 5 mm distance from the entrance to the water cell, for selected Bessel beam orders. The radial part of

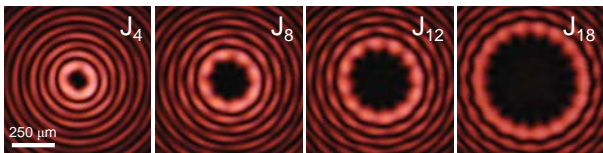


Fig. 3. Selected higher-order Bessel beams at low intensity. The ring intensity features of the beams are modulated due to the  $2\pi$  - *modulo* phase mask.

the phase modulation imposed by the SLM, for all cases shown, is such that the total phase shift from the center of the beam to the edge equals  $100 \cdot \pi$ . The azimuthal component of the modulation varies depending on the beam order according to (1). The peak power of the laser pulses is substantially below the self-focusing threshold, thus the beams propagate in the linear regime.

It is evident that the ring intensity features of the beams, which are supposed to be smooth for the case of ideal Bessel beams, are modulated. There are exactly  $n$  intensity beads (or hot spots) along the circumference of the ring intensity features of the beam of  $n^{\text{th}}$  order. The broadband nature of the incident light coupled to the wavelength dependence of the SLM, the offset in the calibration wavelength of the SLM with respect to the center wavelength of the laser source, as well as a small unmodulated content in the beam may all be contributors to this beaded beam structure. We have confirmed, however, that in our case the beading is predominantly caused by the fact that the modulation phase imposed by the SLM is defined *modulo*  $2\pi$ . The azimuthal component of the phase modulation for the  $n^{\text{th}}$ -order beam experiences exactly  $n$   $2\pi$ -jumps along the circumference of the beam. Thus the phase is not defined at these  $n$  equidistantly spaced jump points, causing the resulting beam pattern to have  $n$  regularly spaced hot spots on its dominant intensity features. The peak-to-peak amplitude of the intensity modulation of the dominant ring, relative to its mean value, is between 10% and 20%, depending on the beam order.

When the pulse energy is increased, distinct filaments start forming on the dominant intensity rings of the beams. The self-focusing collapse is accompanied by the emission of the forward-propagating white-light continuum radiation [1]- [3]. In the top row of Figure 4, the white-light continuum is imaged at the pulse-energy levels when filamentation starts to occur at a 5 mm distance

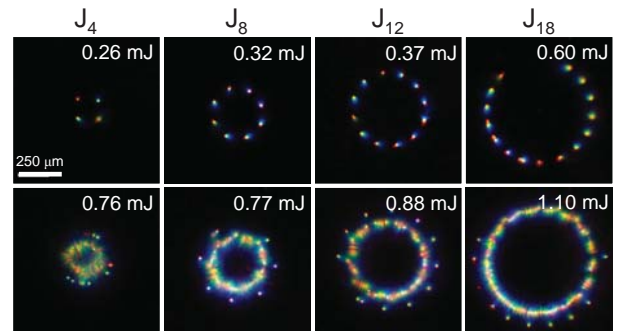


Fig. 4. Top row: Images of the white light emission at the pulse-energy levels corresponding to the onset of filamentation at 5 mm from the entrance to the water cuvette, for selected higher-order Bessel beams. Bottom row: Same at the energy levels corresponding to the onset of filamentation in the secondary ring intensity features.

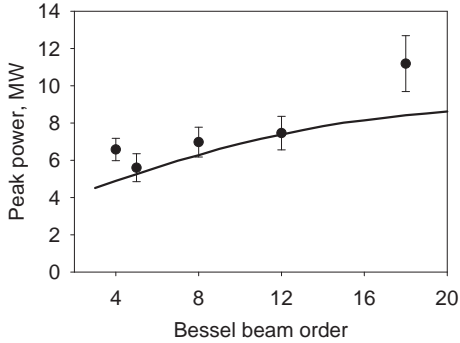


Fig. 5. Critical power for filamentation for higher-order Bessel beams. Experimental data points are shown with circles. The solid line is the result of the calculation based on the adaptation of the Marburger's formula.

from the entrance to the water cell. These images are taken through a color-glass filter that allows visible light to pass through but blocks the pump light at 800 nm.

If the dominant rings of the Bessel beams were perfectly smooth,  $2n + 1$  filaments would be expected to form on the main ring of the  $n^{\text{th}}$ -order beam due to the azimuthal modulation instability [7, 12]. However, in our case, the placement of filaments is forced by the beaded structure of the beams, causing the  $n^{\text{th}}$ -order beam to have exactly  $n$  filaments on its dominant ring. As the pulse energy is increased further, filaments start forming on the secondary rings of the beams, as shown in the bottom row of Figure 4.

For bell-shaped beams, the peak power threshold  $P_{th}$  for filamentation, at a particular distance  $L_c$ , can be relatively accurately estimated by using the semi-empirical Marburger's formula [13]:

$$L_c = \frac{0.367\pi n_0 w_0^2}{\lambda_0 \sqrt{[(P_{th}/P_{cr})^{1/2} - 0.852]^2 - 0.0219}}, \quad (2)$$

where  $w_0$  is the input beam radius,  $\lambda_0$  is the wavelength of the pump beam in vacuum,  $n_0$  is the linear refractive index of the medium, and  $P_{cr}$  is the critical power for self-focusing at infinity. This formula can be adapted for the estimation of the filamentation thresholds for higher-order Bessel beams at a particular propagation distance. In our case, the power in the dominant intensity ring of the  $n^{\text{th}}$ -order beam is approximately equally partitioned between the  $n$  formed filaments, and  $w_0$  approximately equals to the half-width of the ring. The fraction of power in the center ring is deduced from the numerical solution of the Fresnel diffraction integral. The result of the calculation following this procedure, for the case of  $L_c = 5$  mm, is shown in Figure 5 with a solid line. The experimental data for selected beam orders is in a reasonably good agreement with the calculation.

As the self-focusing higher-order Bessel beam propagates further into the water cell, the intensity ring features of the beam self-focus as a whole, at the same time

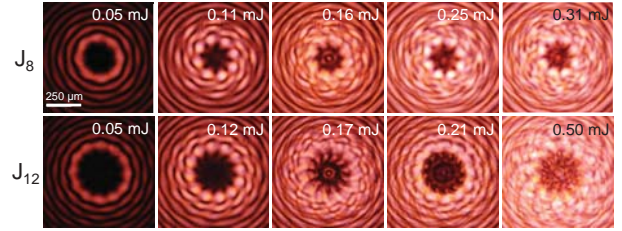


Fig. 6.  $J_8$  (top row) and  $J_{12}$  (bottom row) beams imaged at 50 mm from the entrance to the water cuvette, at various pulse energies.

as the breakup of the rings into individual filaments occurs. In addition, the nonlinear conversion of the conical waves from the incident beam into various spatial wavepackets propagating near the beam axis takes place. A similar effect has been previously reported for the case of self-focusing of the fundamental Bessel beam [14]. Examples of these complex dynamics are shown in Figure 6, for two selected beam orders.

In summary, we have studied the filamentation of femtosecond higher-order Bessel beams in water. Regular filament patterns have been found to form on the dominant intensity rings of the beams. The placement of filaments within the transverse beam profile was dominated by the azimuthal amplitude modulation imposed by the  $2\pi$ -modulo phase mask used to generate the beams. The pulse-energy thresholds for the onset of filamentation, at a particular propagation distance, have been relatively accurately estimated by the adaptation of the Marburger's formula. The nonlinear conversion of the incident conical waves into the localized wave packets propagating near the beam axis has been observed.

The authors acknowledge support from The United States Air Force Office of Scientific Research under programs FA9550-10-1-0237 and FA9550-10-1-0561.

## References

1. A. Couairon, A. Mysyrowicz, *Phys. Rep.* **41**, 47 (2007).
2. L. Bergé *et al.*, *Rep. Prog. Phys.* **70**, 1633 (2007).
3. S. L. Chin, *Femtosecond Laser Filamentation* (Springer, 2010).
4. A. Dubietis *et al.*, *Opt. Express* **15**, 4168 (2007).
5. P. Polynkin *et al.*, *Opt. Express* **16**, 15733 (2008).
6. M. Bigelow, P. Zerom, R. Boyd, *Phys. Rev. Lett.* **92**, 083902 (2004).
7. L. Vuong *et al.*, *Phys. Rev. Lett.* **96**, 133901 (2006).
8. T. Grow *et al.*, *Phys. Rev. Lett.* **99**, 133902 (2007).
9. P. Polynkin *et al.*, *Science* **324**, 229 (2009).
10. P. Polynkin, M. Kolesik, J. Moloney, *Phys. Rev. Lett.* **103**, 123902 (2009).
11. C. Paterson, R. Smith, *Opt. Commun.* **124**, 121 (1996).
12. A. Vinçotte, L. Bergé, *Phys. Rev. Lett.* **95**, 193901 (2005).
13. J. Marburger, *Prog. Quant. Electr.* **4**, 35 (1975).
14. R. Gadonas *et al.*, *Opt. Commun.* **196**, 309 (2001).

## Full References

- [1] A. Couairon and A. Mysyrowicz, “Femtosecond filamentation in transparent media”, *Physics Reports* **441**, pp. 47-189 (2007).
- [2] L. Bergé, S. Skupin, R. Nuter, J. Kasparian, and J.-P. Wolf, “Ultrashort filaments of light in weakly ionized, optically transparent media”, *Reports on Progress in Physics* **70**, pp. 1633-1713 (2007).
- [3] S. L. Chin, *Femtosecond Laser Filamentation* (Springer, 2010).
- [4] A. Dubietis, P. Polesana, G. Valiulis, A. Stabinis, P. Di Trapani, A. Piskarkas, “Axial emission and spectral broadening in self-focusing of femtosecond Bessel beams”, *Optics Express* **15**, pp. 4168-4175 (2007).
- [5] P. Polynkin, M. Kolesik, A. Roberts, D. Faccio, P. Di Trapani, J. Moloney, “Generation of extended plasma channels in air using femtosecond Bessel beams”, *Optics Express* **16**, pp. 15733-15740 (2008).
- [6] M. Bigelow, P. Zerom, R. Boyd, “Breakup of Ring Beams Carrying Orbital Angular Momentum in Sodium Vapor”, *Physical Review Letters* **92**, p. 083902 (2004).
- [7] L. Vuong, T. Grow, A. Ishaaya, A. Gaeta, G. W. 't Hooft, E. Eliel, G. Fibich, “Collapse of Optical Vortices”, *Physical Review Letters* **96**, p. 133901 (2006).
- [8] T. Grow, A. Ishaaya, L. Vuong, A. Gaeta, “Collapse and Stability of Necklace Beams in Kerr Media”, *Physical Review Letters* **99**, p. 133902 (2007).
- [9] P. Polynkin, M. Kolesik, J. Moloney, G. Siviloglou, D. Christodoulides, “Curved Plasma Channel Generation Using Ultraintense Airy Beams”, *Science* **324**, pp. 229-232 (2009).
- [10] P. Polynkin, M. Kolesik, J. Moloney, “Filamentation of Femtosecond Laser Airy Beams in Water”, *Physical Review Letters* **103**, p. 123902 (2009).
- [11] C. Paterson, R. Smith, “Higher-order Bessel waves produced by axicon-type computer-generated holograms”, *Optics Communications* **124**, pp. 121-130 (1996).
- [12] A. Vinçotte, L. Bergé, “Femtosecond Optical Vortices in Air”, *Physical Review Letters* **95**, p. 193901 (2005).
- [13] J. Marburger, “Self-focusing: Theory”, *Progress in Quantum Electronics* **4**, pp. 35-110 (1975).
- [14] R. Gadonas, V. Jarutis, R. Paškauskas, V. Smilgevičius, A. Atabinis, V. Vaičaitis, “Self-action of Bessel beam in nonlinear medium”, *Optics Communications* **196**, pp. 309-316 (2001).

# Supercontinuum Generation with Femtosecond Self-Healing Airy Pulses

Craig Ament, Pavel Polynkin,\* and Jerome V. Moloney  
*College of Optical Sciences, The University of Arizona, Tucson, Arizona 85721, USA*  
 (Dated: July 5, 2011)

We report experiments and numerical simulations on supercontinuum generation with femtosecond Airy pulses in a highly nonlinear optical fiber. The ability of the Airy waveform to regenerate its dominant intensity peak results in the generation of distinct spectral features. Airy pulses and other self-healing temporal waveforms may be useful for the generation of spectra with desired properties.

PACS numbers: 42.65.Re, 42.81.Dp

The dramatic spectral broadening experienced by intense optical pulses in nonlinear media, commonly known as supercontinuum generation, is a result of the complex interplay between linear dispersion and instantaneous and delayed nonlinearity in the medium [1]. Microstructured optical fibers are particularly well suited for supercontinuum generation because the nonlinearity and dispersion landscape in microstructured fibers can be altered by the design of the waveguide structure [2].

Although supercontinuum generation in optical fibers has been extensively studied under a vast variety of conditions in the past (for a review, see, for example, [3]), the overwhelming majority of prior studies utilized intense optical pulses with bell-shaped temporal profiles. There have been several reports on the optimization of supercontinuum generation via pulse shaping [4] - [6]. However, this approach remains insufficiently explored.

Recently, a new kind of optical pulse has been introduced to optics [7]. These so-called Airy pulses have their field envelopes described in terms of truncated or apodized Airy functions of time. These pulses are temporal analogues of Airy beams, also introduced in [7]. Like Airy beams resist diffraction and self-bend, Airy pulses resist dispersion and their dominant intensity peaks accelerate on propagation. Another important property of Airy pulses is their ability to regenerate their dominant intensity features should those features be selectively attenuated or distorted. All of the above features are linear effects. The dispersion resistance and self-regeneration of the temporal Airy wavepacket are illustrated by simulations shown in Figure 1. Temporal Airy pulses have been experimentally realized and their properties have been studied in both linear [8] and nonlinear [9] regimes.

The ability of Airy pulses to self-heal makes them potentially useful in the context of supercontinuum generation. With an input bell-shaped pulse and in the anomalous dispersion regime, which is commonly used for the generation of broadest continua, the spectral evolution of the pulse largely ends when the pulse is transformed into one or several fundamental solitons. The excess energy in this case is shed in the form of dispersive waves [10]. The placement of these features in the spectrum is determined by the dispersion landscape of the fiber. In the case of the self-healing Airy pulse, the generation of new spectral components may continue after the dominant peak of the waveform has produced solitons and dispersive waves

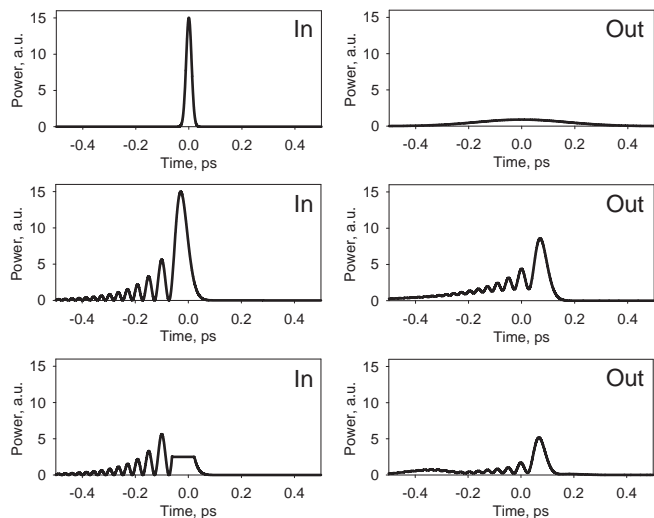


FIG. 1: Top row: Input and output temporal intensity profiles of a Gaussian pulse propagating in a linear dispersive optical fiber that has a second-order dispersion only. The 24 fs-long input pulse is severely dispersed on propagation. Middle row: The input pulse is an exponentially apodized Airy pulse with the same optical bandwidth as that of the Gaussian pulse above. Propagation through the same fiber leaves the dominant peak of the waveform largely intact. Bottom row: The dominant intensity peak of the input Airy pulse is cutoff at a level of one-sixth of the peak value. The feature is restored on propagation through the same fiber as above.

and removed itself from the continuum-generation process. Under the right conditions, the dominant feature of the Airy waveform will be regenerated. At that point, it will propagate with a velocity different from that of the dominant peak of the original pulse, affecting the placement of the newly generated spectral components. Thus the use of Airy pulses and other sophisticated self-healing temporal waveforms for continuum generation may allow for control over the generated spectrum by linear optic means.

In this Letter, we report the results of a numerical and experimental study of supercontinuum generation with Airy pulses in a microstructured optical fiber. Our results show that the self-healing property of the pulse, under certain conditions, results in nontrivial cyclic behavior. The dominant feature of the pulse creates a soliton-

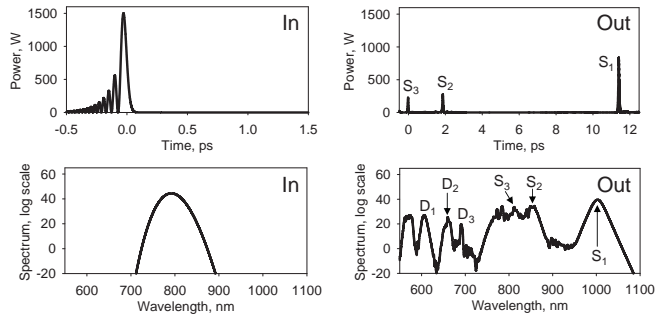


FIG. 2: Top row: Input and output temporal waveforms for the case of the propagation of an Airy pulse with  $-60,000 \text{ fs}^3$  cubic spectral phase in a 1 m-long nonlinear fiber with the parameters described in the text. Bottom row: Corresponding spectra. Solitons and dispersive waves are marked with letters  $S_i$  and  $D_i$ , where the subscript indicates the order of appearance of these features.

dispersive wave pair, regenerates itself through the self-healing action of the Airy pulse, then creates another soliton-dispersive wave pair, and so on. Such propagation dynamics results in the generation of distinct features in the output optical spectrum.

An Airy pulse is created by imposing a cubic phase onto the spectrum of an input Gaussian pulse. The cubic phase can be either positive or negative, which corresponds to the Airy pulse with the tail lagging behind the dominant peak of the pulse or vice versa. The Airy pulse shown in Figure 1 has a negative value of the cubic spectral phase. Accordingly, the tail of the waveform in this case is propagating in front of the dominant peak.

The orientation of the tail of the pulse with respect to the pulse waveform has two important consequences. First, linear third-order dispersion, which has a particular sign, will add to or subtract from the cubic phase of the input Airy pulse, resulting in the extension or reduction of the dispersion-resistant propagation range of the pulse. In fact, the generation of temporal Airy waveforms from input Gaussian pulses, as a result of propagation through a fiber with third-order dispersion, has been described as early as 1979 [11], much before the concept of the dispersion-resistant Airy pulse had been proposed. Second, solitons produced through the collapse of the dominant peak of the Airy pulse generally tend to lag behind the main pulse waveform. Thus for the case when the tail propagates ahead of the main peak of the pulse, the generated solitons cleanly detach themselves from the waveform and leave the self-healing of the pulse unaffected. When the tail of the pulse propagates behind its main peak, the generated solitons pass through the tail and interfere with the self-healing.

The parameters of the optical fiber used in the simulations throughout this report closely match those of the fiber used in our experiments. The model fiber has the nonlinear coefficient  $\gamma$  equal to  $0.11 (\text{W}\cdot\text{m})^{-1}$ , zero-dispersion wavelength of 745 nm, and the maximum group-velocity dispersion of  $240 \text{ ps}/\text{nm}\cdot\text{km}$ , which occurs

at  $1.96 \mu\text{m}$  wavelength. The fiber dispersion is anomalous for all wavelengths above 745 nm. At 800 nm, which is the center wavelength of the input pulses, the value of dispersion is  $35 \text{ ps}/\text{nm}\cdot\text{km}$ . The dispersion profile of the model fiber is fitted by a 10-order polynomial in optical frequency.

The input Airy pulses are numerically generated by imposing a cubic spectral phase of minus or plus  $60,000 \text{ fs}^3$ , onto the spectrum of a 24 fs-long, transform-limited Gaussian pulse. Under these conditions, the dominant peak of the pulse contains about one half of the total energy of the waveform. The pulse evolution is simulated by using the numerical model adapted from [12]. In the model, the optical field is assumed to remain linearly polarized throughout the entire propagation in the fiber.

Figure 2 shows the temporal and spectral outputs from a 1 m-long nonlinear fiber with the parameters listed above, for the case of an input Airy pulse with peak power of 1.5 kW and a negative cubic spectral phase equal to  $-60,000 \text{ fs}^3$ . The tail of the waveform in this case propagates in front of its main peak. Three soliton-formation events are evident from the side-by-side examination of the temporal and spectral shapes of the pulse as it propagates through the fiber. All three solitons are produced through the reshaping of the main intensity peak of the Airy pulse, which recreates itself after each soliton-formation event. The spectral features corresponding to the generated solitons and dispersive waves are marked in the Figure by letters  $S_1$ - $S_3$  and  $D_1$ - $D_3$ , where the subscript indicates the order of appearance of these features. After their formation, solitons and dispersive waves remain essentially invariant on propagation, except for the continuous frequency red shifting of the soliton spectral peaks caused by higher-order dispersion and delayed Raman nonlinearity.

The red-shifted solitons gradually slow down and may catch up with dispersive waves in time domain. In that case, the cross-phase modulation induced by the intense soliton field causes the redistribution of the energy of the dispersive wave and results in the appearance of an additional blue-shifted spectral peak, as described in [13]. The left-most peak at 570 nm in the bottom right panel of Figure 2 is the result of such an interaction between the first emitted soliton  $S_1$  and the dispersive wave  $D_1$ .

The placement of the spectral peak corresponding to a particular dispersive wave is determined by the wave-number matching between the dispersive wave and the higher-order soliton that undergoes fission, in the immediate vicinity of the point where the peak power of the soliton is the highest [14]. For the case of a fundamental soliton, the matching condition has the following form:

$$\sum_{n \geq 2} \frac{\beta_n(\omega_S)}{n!} (\omega_D - \omega_S)^n = \frac{\gamma P_S}{2}, \quad (1)$$

where  $\beta_n(\omega_S)$  are the higher-order dispersion coefficients of the fiber at  $\omega_S$ , the optical frequency of the soliton,  $\omega_D$  is the center frequency of the dispersive wave,  $\gamma$  is the

nonlinear parameter of the fiber, and  $P_S$  is the soliton peak power. Although (1) is only valid for fundamental solitons, it is frequently used for estimations of the dispersive wave placement in the cases of solitons of higher order. The center wavelengths of the three generated dispersive waves in the case shown in Figure 2 are, in order of their appearance, 600 nm, 668 nm, and 690 nm. The estimates based on the formula (1) are 580 nm, 639 nm, and 663 nm. These estimates are consistently lower than the values derived from the simulations. The poor agreement may be caused by, among other things, the accelerating nature of the Airy waveform, for which case the condition (1) is overly simplified.

Figure 3 provides a closer look at the first two soliton-formation events. The top left panel shows the temporal profile of the pulse after it propagated 6 cm through the fiber. At that point, the main peak of the input pulse has transformed itself into a higher-order soliton that subsequently underwent fission and shed a dispersive wave. The main peak of the waveform is nearly regenerated and ready to produce another soliton. The top right panel shows the pulse profile after 16 cm of propagation. The regenerated main peak of the Airy pulse has just created another soliton.

In the spectral domain, the soliton and dispersive wave created through the first collapse of the main Airy peak are straightforwardly identifiable at both 6 cm and 16 cm. Spectral features resulting from the second soliton-formation event are not as obvious. To properly identify them, we computed a Fourier transform of the portion of the temporal waveform at 16 cm that contained the peak marked by  $S_2$ .

In the above example, the Airy pulse had a negative value of the cubic spectral phase, in which case the tail of the Airy waveform propagated in front of its main peak. The solitons and dispersive waves generated from the main peak of the pulse lagged behind the waveform and did not interfere with its ability to self-regenerate.

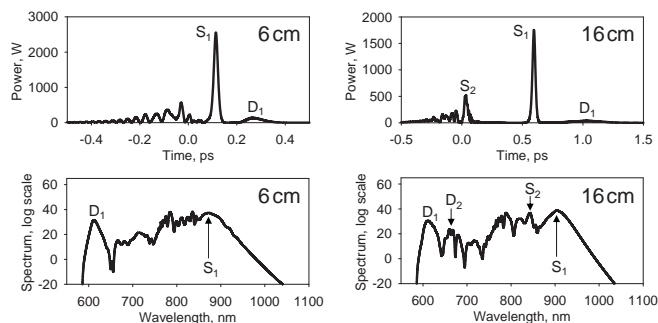


FIG. 3: Top row, left: Temporal waveforms of the Airy pulse with  $-60,000 \text{ fs}^3$  cubic spectral phase after 6 cm propagation in the fiber. The main peak of the Airy waveform has produced a soliton-dispersive wave pair and is nearly regenerated. Right: Same after 16 cm propagation. The regenerated main peak of the pulse has produced another soliton-dispersive wave pair. Bottom row: Corresponding spectra.

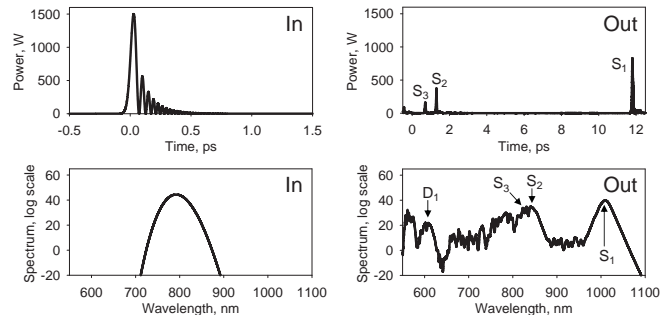


FIG. 4: Input Airy pulse with  $+60,000 \text{ fs}^3$  cubic spectral phase propagates in 1 m-long nonlinear fiber. Top row: Temporal input and output waveforms. Bottom row: Corresponding spectra. Only one distinct dispersive-wave peak is produced.

The case corresponding to the same value but opposite sign of the cubic spectral phase is shown in Figure 4. As in the previous case, the dominant intensity peak of the input Airy pulse relatively quickly reshapes itself into a higher-order soliton which subsequently morphs into a fundamental soliton and emits a dispersive wave. However, in this case, the generated soliton passes through the tail of the Airy pulse and perturbs the phase of this waveform via cross-phase modulation. As a result of that perturbation, the Airy waveform loses its ability to regenerate its main peak. Two additional solitons are still produced by the remaining part of the pulse, but these features originate from the secondary peaks of the waveform, and not from the rebuilt dominant intensity feature. Only one distinct dispersive-wave peak is evident in the output spectrum in this case. As in the case with negative cubic phase, the leftmost feature in the output spectrum results from the interaction of the first emitted soliton with its own dispersive wave.

In order to validate the pulse propagation scenario put forth above by numerical simulations, we conducted experiments on supercontinuum generation with Airy pulses in a nonlinear fiber. In the experiments, the input Gaussian pulses are generated by a commercial mode-locked Ti:Sapphire laser oscillator operating at 800 nm center wavelength and 80 MHz pulse repetition frequency. Pulses out of the oscillator are de-chirped to about 24 fs duration, which is close to the transform limit, using a dispersive prism pair. Airy pulses are produced by imposing a cubic spectral phase onto these transform-limited Gaussian pulses, using a commercial computer-controlled pulse shaper (Silhouette<sup>TM</sup> by Coherent). The maximum cubic phase attainable in our setup is limited to plus or minus  $60,000 \text{ fs}^3$ , which matches the magnitude of the cubic phase used in the simulations. The temporal profile of the shaped pulses is analyzed using a commercial FROG system.

The shaped pulses are coupled into a 1 m-long nonlinear fiber with the parameters that closely match those used in the computer simulations discussed above. The mode-field diameter of the fiber is about  $1.4 \mu\text{m}$ , its es-

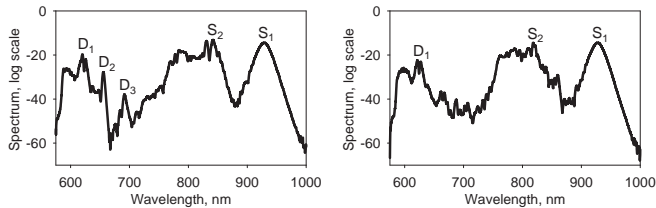


FIG. 5: Supercontinuum spectra recorded at the output of a 1 m-long microstructured fiber with the parameters closely matching those used in the simulations. The case with the input Airy pulse with a negative cubic spectral phase equal  $-60,000 \text{ fs}^3$  (left) results in the generation of three distinct dispersive-wave features. The case with the same but opposite spectral phase (right) results in the generation of only one distinct dispersive wave.

estimated nonlinear coefficient  $\gamma$  equals  $105 (\text{W}\cdot\text{m})^{-1}$ , and the zero dispersion wavelength of the fiber is 745 nm. The coupling efficiency of the shaped laser pulses into the fiber in our setup is about 20%, which corresponds to 0.25 nJ of maximum pulse energy coupled into the fiber. The input pulse energy is varied by adjusting the focusing of the fiber-coupling arrangement. The supercontinuum spectra at the output from the fiber are recorded using an optical spectrum analyzer.

Two examples of experimentally measured spectra are shown in Figure 5. In both cases shown, the energy of input Airy pulses equals 0.12 nJ. The amount of the cubic spectral phase imposed by the pulse shaper in order to generate these waveforms is  $-60,000 \text{ fs}^3$  (left) and  $+60,000 \text{ fs}^3$  (right). Under these conditions, the estimated peak power of the Airy pulses coupled into the fiber is 1.5 kW, matching the value used in the simulations.

For the case with a negative cubic spectral phase, the generated supercontinuum spectrum has three distinct and approximately equidistant dispersive wave peaks, in qualitative agreement with the simulation shown in Figure 2. For the case with a positive cubic phase, only one distinct dispersive-wave feature is produced, again in agreement with the simulations. In both cases, the left-most peak in the spectrum is due to the interaction between the first emitted soliton and its own dispersive wave. The quantitative discrepancy between the experimental results and the simulations is likely due to the incomplete knowledge of the fiber parameters as well as to the residual fiber birefringence, which was not accounted for in our model.

In conclusion, we conducted experiments and numerical simulations on supercontinuum generation with self-healing Airy pulses in a highly nonlinear fiber. The pulse propagation dynamic is found to be different for the cases when the tail of the Airy waveform propagates in front of and behind the main peak of the pulse. In the first case, the dominant peak of the pulse recreates itself after several soliton formation events, resulting in the generation of distinct dispersive-wave features in the output spectrum. In the second case, the soliton generated from the first collapse of the main peak of the pulse passes through the tail of the waveform and disrupts its ability to self-regenerate. The results of the modeling are in qualitative agreement with the experiments.

The authors acknowledge helpful discussions with Miroslav Kolesik. This work was supported by The United States Air Force Office of Scientific Research under programs FA9550-10-1-0237 and FA9550-10-1-0561.

\* Electronic address: [ppolykin@optics.arizona.edu](mailto:ppolykin@optics.arizona.edu)

- 
- [1] *The Supercontinuum Laser Source: Fundamentals with Updated References*, edited by R. Alfano (Springer, New York, 2006).
  - [2] T. Birks, W. Wadsworth, P. Russell, *IEEE Photon. Technol. Lett.* **11**, 674 (1999).
  - [3] *Supercontinuum Generation in Optical Fibers*, Edited by J. Dudley and J. Taylor (Cambridge Univ. Press, 2010).
  - [4] S. Xu, D. Reitze, R. Windeler, *Opt. Express* **12**, 4731 (2004).
  - [5] B. von Vacano, W. Wohlleben, M. Motzkus, *Opt. Lett.* **31**, 413 (2006).
  - [6] D. Lorenc, D. Velic, A. Markevitch, R. Levis, *Opt. Commun.* **276**, 288 (2007).
  - [7] G. Siviloglou, J. Broky, A. Dogariu, D. Christodoulides, *Phys. Rev. Lett.* **99**, p. 213901 (2007).
  - [8] A. Chong, W. Renninger, D. Christodoulides, F. Wise, *Nature Photonics* **4**, 103 (2010).
  - [9] D. Abdollahpour, S. Suntsov, D. Papazoglou, S. Tzorzakis, *Phys. Rev. Lett.* **105**, 253901 (2010).
  - [10] A. Husakou, J. Herrmann, *Phys. Rev. Lett.* **87**, 203901 (2001).
  - [11] M. Miyagi, S. Nishida, *Appl. Opt.* **18**, 2237 (1979).
  - [12] J. Travers, M. Frosz, J. Dudley, “Nonlinear fibre optics overview”, in [3], p. 46.
  - [13] G. Genty, M. Lehtonen, H. Ludvigsen, *Opt. Express* **12**, 4614 (2004).
  - [14] D. Austin, C. M. de Sterke, B. Eggleton, *Opt. Express* **14**, 11997 (2006).

# Third and fifth harmonics generation by tightly focused femtosecond pulses at $2.2\ \mu\text{m}$ wavelength in air

Gombojav O. Ariunbold, Pavel Polynkin,\* and Jerome V. Moloney

*College of Optical Sciences, The University of Arizona, Tucson, Arizona 85721, USA*

*\*Corresponding author: ppolynkin@optics.arizona.edu*

Compiled June 22, 2011

We report experiments on the generation of third and fifth harmonics of millijoule-level, tightly focused, femtosecond laser pulses at  $2.2\ \mu\text{m}$  wavelength in air. The measured ratio of yields of the third and fifth harmonics in our setup is about  $2 \cdot 10^{-4}$ . This result contradicts the recent suggestion that the Kerr effect in air saturates and changes sign in ultra-intense optical fields. © 2011 Optical Society of America

*OCIS codes:* 190.2620, 190.3270, 320.7110

Linear and nearly instantaneous dependence of the refractive index of transparent media on the intensity of the optical field is the essence of the electronic Kerr effect, which is the cornerstone of nonlinear optics. In a recent publication, it has been suggested that the notion of the instantaneous electronic Kerr effect must be generalized [1]. Measurements of the transient birefringence induced in various gases by ultraintense and ultrashort optical pulses have been interpreted as the saturation and sign reversal of the nonlinear refractive index at the optical intensity levels on the order of several tens of terawatts per square centimeter. The common linear dependence of the index of refraction on the intensity of the optical field has been amended by the inclusion of new, nontrivially large terms proportional to second and higher powers of intensity.

The field of femtosecond laser filamentation is probably the one that would be affected the most, should the above suggestion be proven valid. For many years, it was believed that the intrinsically unstable balance between diffraction and self-focusing in ultraintense laser beams undergoing filamentation in gaseous media is stabilized by the weak defocusing action of plasma generated on the beam axis via multi-photon ionization [2] – [4]. The higher-order Kerr terms, if they did exist, could provide for an alternative stabilization mechanism. The filament propagation would be much longer ranged, as the losses to ionization would be reduced compared to the established filamentation scenario based on plasma defocusing [5].

Effects associated with weak saturation of the electronic Kerr response have been considered in the context of laser filamentation previously [6] – [8]. However, the suggestion that the Kerr effect may reverse sign and cause, among other things, beam self-defocusing, were too radical a departure from the established framework of laser filamentation and nonlinear optics in general. Almost immediately after the publication of [1], the results reported in that paper became the subject of intense debates.

Following [9], we will refer to the claim put forth in [1]

as the Higher-Order Kerr Effect (HOKE) theory. Several independent experimental tests of HOKE in the context of laser filamentation have unambiguously proven that even if the higher-order Kerr terms do exist, they are not operative in common laser filaments in gases [10] – [12]. The question still remains whether this high-order Kerr effect exists at all. It has been argued that the sign reversal of the Kerr effect may occur in a transient regime, while neutral molecules in the gas are undergoing multiphoton ionization [13], [14].

Very recent experiments on direct profiling of the cross-phase modulation response in a thin gas target illuminated by an ultraintense and ultrashort laser pulse revealed no evidence of even a transient saturation of the Kerr effect, in complete contradiction with HOKE [15]. An alternative test that would also look at the presence of a potentially transient HOKE response has been proposed in [16]. In this Letter, we report experimental results on the realization of that proposal. In agreement with [15], we found no evidence of the higher-order Kerr response. We believe that at this time, the combined body of experimental evidence is sufficient to permanently disqualify the HOKE paradigm.

The experimental test reported here is based on the dramatic effect that the inclusion of the HOKE terms would have on the efficiency of third and fifth harmonic generation by a femtosecond laser pulse with peak power in the vicinity of the alleged turnover point for the higher-order Kerr effect. As has been numerically shown in [16] for tightly focused femtosecond pulses at  $1.3\ \mu\text{m}$  wavelength, the ratio of the yields of the fifth and third harmonics generated by such pulses is a growing function of the intensity of the pulse. This ratio saturates at a value on the order of one if the HOKE terms are included in the model, and it remains very small ( $\sim 10^{-4}$ ) when these terms are omitted. Such a dramatic difference between the predictions of the two models is the consequence of the fact that in the established approach, the fifth harmonic generation is a cascade process involving the nonlinear mixing between the already generated third harmonic and the leftover pump, while in the new

theory, the fifth harmonic is generated directly from the fundamental through the higher-order Kerr response.

The above qualitative difference between the predictions of the old and the new models makes the comparison of yields of the third and fifth harmonics a reliable test of the new theory that is largely insensitive to the variations of the material parameters and to a particular experimental geometry.

We point out that an experiment on the generation of third and fifth harmonics in an Argon cell using intense pump pulses at 800 nm wavelength has been reported much before the HOKE controversy had even emerged [17]. The results of that work have been recently used to argue in favor of the validity of HOKE [18]. In our view, [17] is not straightforwardly applicable to the resolution of the HOKE controversy for the following reasons. Experiments reported in [17] were certainly not designed to support or disprove the HOKE theory, which was nonexistent at the time when [17] was published. Instead, that work targeted the demonstration of highest possible yield of fifth harmonic. The wavelength of the generated fifth harmonic was about 162 nm, which is in vacuum UV, thus making its reliable and quantitative characterization not straightforward. Furthermore, the extended interaction length and the associated phase mismatch between the pump wavelength and the generated harmonics, together with the fact that the actually detected portions of the harmonics were not exactly known, made the interpretation of those experiments in the context of the resolution of the HOKE controversy not reliable.

The experiment reported here is free from the above complications. In our case, third and fifth harmonics are generated using millijoule-level femtosecond laser pulses at  $2.2\ \mu\text{m}$  wavelength. This choice of pump wavelength is dictated by three considerations. First, both third and fifth harmonics of this wavelength fall into the near UV – visible spectral range, making them easily detectable. Second, the phase-matching distance between the pump beam and both of the harmonics in air at normal atmospheric pressure, at this pump wavelength, is estimated at over 10 centimeters. Thus using a short interaction length of less than 1 centimeter in our experiment eliminates any potential issues associated with phase mismatch between the pump and the harmonics. Third, the effect of the higher-order Kerr terms, according to [14], should become even more pronounced in the mid-infrared, compared to the 800 nm wavelength range commonly used in the high-intensity femtosecond laser experiments.

Our experimental setup is schematically shown in Figure 1. Femtosecond pulses at  $2.2\ \mu\text{m}$  center wavelength are produced by a commercial high-energy Optical Parametric Amplifier (OPA, Palitra-HE model by Quantronix Corporation). The OPA is pumped by about 40 fs-long, 20 mJ pulses at 800 nm wavelength generated by an ultrafast Ti:Sapphire amplifier chain operating at a 10 Hz pulse repetition frequency. The OPA is tuned to

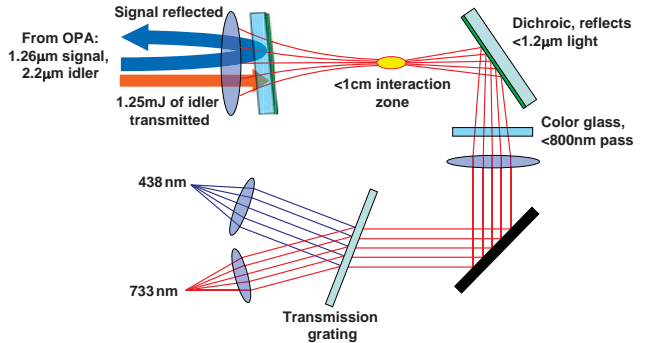


Fig. 1. (Color online) Schematic of the experimental setup.

produce signal and idler pulses at  $1.26\ \mu\text{m}$  and  $2.20\ \mu\text{m}$  center wavelengths, respectively. The output beam from the OPA has a diameter of about 10 mm. Both signal and idler pulses have energies of about 1.5 mJ. The duration of the pulses is estimated by the OPA manufacturer at between 40 and 60 fs [19].

The co-propagating signal and idler beams are focused by a lens with 20 cm focal length. Immediately after the lens, the  $1.26\ \mu\text{m}$  signal is reflected by a dichroic beam-splitter operated at near normal incidence. This dichroic (CVI – Melles Griot Corporation, part number BBDS), is a dielectric low-pass filter. At normal incidence, it has a transmission cutoff at the wavelength of about  $1.3\ \mu\text{m}$ . The idler pulse at  $2.2\ \mu\text{m}$  is transmitted by this mirror with about 90% efficiency, while the transmission for the signal beam at  $1.26\ \mu\text{m}$  is less than 0.1%. For all wavelengths below  $1\ \mu\text{m}$ , transmission is less than 0.05%.

The energy of the focused  $2.2\ \mu\text{m}$  idler pulse, after the dichroic, is measured at about 1.25 mJ. It is important that the dichroic is oriented with its substrate facing the incident beam. In this case, the visible and UV light possibly generated inside the substrate is reflected by the coating, and only the  $2.2\ \mu\text{m}$  idler pulse is passed into the interaction zone.

The third and fifth harmonics of the  $2.2\ \mu\text{m}$  pump are generated in the ambient air, near the focal plane of the focusing lens. The estimated intensity of the pump beam near the focus is above the turnover point for the alleged sign reversal of the Kerr effect in the HOKE model and also above the ionization threshold of air. The length of the short and faint plasma spark generated in the vicinity of the interaction zone is less than 1 cm. Under these conditions, the ratio of the third and fifth harmonic yields, according to the HOKE theory, should approach one.

The third and fifth harmonics of the pump are reflected by another dichroic mirror, which is identical to the one used to block the signal pulse at  $1.26\ \mu\text{m}$  from the OPA. The second dichroic is operated with the coating facing the incident beam and at a  $45^\circ$  angle of incidence. This mirror efficiently reflects the generated harmonics, but blocks over 90% of the  $2.2\ \mu\text{m}$  pump. The

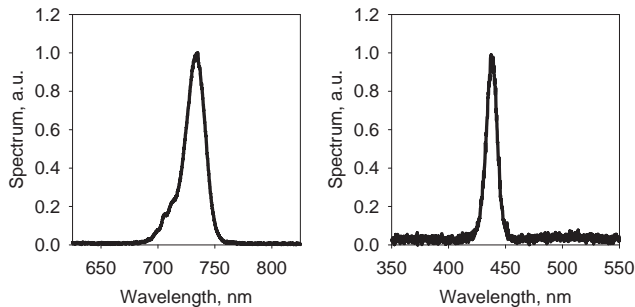


Fig. 2. Normalized spectra of third harmonic (left) and fifth harmonic (right) generated by tightly focused femtosecond pulses at  $2.2\ \mu\text{m}$  wavelength in air, on linear scale.

residual pump is further attenuated by about five orders of magnitude by a 3 mm-thick color-glass filter plate (KG5 filter by Schott Glass Corporation) placed after the dichroic.

After collimation with another lens, the signals at third and fifth harmonics are spatially separated by a 300 lines per millimeter transmissive diffraction grating. The spectra of the two harmonics are recorded by a fiber-coupled spectrometer (model USB4000 by Ocean Optics Corporation), with the aid of two additional lenses that separately focus the harmonic beams after they are separated by the grating. These spectra are shown in Figure 2. They are centered at 733 nm and 438 nm, very close to one-third and one-fifth of the pump wavelength of  $2.20\ \mu\text{m}$ .

The emission bandwidths of the detected third and fifth harmonics are about 20 nm and 11 nm, respectively. Assuming that the harmonic pulses are both Gaussian and close to transform limit, the durations of the two pulses can be estimated as 40 fs and 25 fs. The ratio of these pulse durations is in the ballpark of  $\sqrt{5/3}$ , which would be expected in the case of the perfectly phase-matched harmonic generation with non-depleted pump.

The energies of the two harmonic pulses are measured by dedicated silicon detectors that were calibrated against a pyroelectric detector, using reference laser pulses at 800 nm wavelength. Accounting for all losses experienced by the generated harmonics in our setup, the energies of the third and fifth harmonics are found equal to  $1.9\ \mu\text{J}$  and  $0.4\ \text{nJ}$ , respectively. These pulse energies correspond to yields of about  $1.5 \cdot 10^{-3}$  for third harmonic and  $3.0 \cdot 10^{-7}$  for fifth harmonic, with respect to the energy of the pump pulse at  $2.2\ \mu\text{m}$  wavelength in the interaction zone. The ratio of yields for the two harmonics is about  $2 \cdot 10^{-4}$ , in contradiction with the HOKE theory.

To verify that the generated harmonics were in fact originating from the tightly focused interaction zone and not from any optics in the setup, we substituted the focusing lens with a glass plate with the same thickness as the lens. In that case, the intensities of both third and

fifth harmonics of the pump fell below the detectability limit.

In conclusion, we have conducted a dedicated experiment in order to validate or disprove the existence of the higher-order Kerr effect proposed in [1]. Our test was based on the qualitative difference that the inclusion of the higher-order Kerr terms has on the yields of the third and fifth harmonics generated by tightly focused ultraintense laser pulses at  $2.2\ \mu\text{m}$  wavelength in ambient air. Our results unambiguously disprove the existence of the high-order Kerr response, even in the transient regime. Our conclusion is in agreement with another recently reported dedicated test of HOKE [15].

The authors acknowledge helpful discussion with Miroslav Kolesik. This work was supported by The United States Air Force Office of Scientific Research under programs FA9550-10-1-0237 and FA9550-10-1-0561.

## References

1. V. Loriot, E. Hertz, O. Faucher, and B. Lavorel, *Opt. Express* **17**, 13429 (2009); *Opt. Express* **18**, 3011(E) (2010).
2. A. Couairon and A. Mysyrowicz, *Phys. Rep.* **441**, 47 (2007).
3. L. Bergé, S. Skupin, R. Nuter, J. Kasparian, and J.-P. Wolf, *Rep. Prog. Phys.* **70**, 1633 (2007).
4. S. L. Chin, *Femtosecond Laser Filamentation* (Springer, 2010).
5. P. Bédot, J. Kasparian, S. Henin, V. Loriot, T. Vieillard, E. Hertz, O. Faucher, B. Lavorel, and J.-P. Wolf, *Phys. Rev. Lett.* **104**, 103903 (2010).
6. M. Aközbek, M. Scalora, C. Bowden, and S. L. Chin, *Opt. Commun.* **191**, 353 (2001).
7. A. Couairon, *Phys. Rev. A* **68**, 015801 (2003).
8. A. Vincotte and L. Bergé, *Phys. Rev. A* **70**, 061802 (2004).
9. P. Bédot, E. Hertz, J. Kasparian, B. Lavorel, J.-P. Wolf, and O. Faucher, *Phys. Rev. Lett.* **106**, 243902 (2011).
10. P. Polynkin, M. Kolesik, E. Wright, and J. Moloney, *Phys. Rev. Lett.* **106**, 153902 (2011).
11. O. Kosareva, J.-F. Daigle, N. Panov, T. Wang, S. Hosseini, S. Yuan, G. Roy, V. Makarov, and S. L. Chin, *Opt. Lett.* **36**, 1035 (2011).
12. Y.-H. Chen, S. Varma, T. Antonsen, and H. Milchberg, *Phys. Rev. Lett.* **105**, 215005 (2010).
13. A. Teleki, E. Wright, and M. Kolesik, *Phys. Rev. A* **82**, 065801 (2010).
14. C. Bree, A. Demircan, and G. Steinmeyer, *Phys. Rev. Lett.* **106**, 183902 (2011).
15. J. Wahlstrand, Y.-H. Cheng, and H. Milchberg, arXiv:1105.6334.v1.
16. M. Kolesik, E. Wright, and J. Moloney, *Opt. Lett.* **35**, 2550 (2010).
17. K. Kosma, S. Trushin, W. Schmid, and W. Fuss, *Opt. Lett.* **33**, 723 (2008).
18. P. Bédot, E. Hertz, B. Lavorel, J. Kasparian, J.-P. Wolf, and O. Faucher, *Opt. Lett.* **36**, 828 (2011).
19. P. Tzankov, M. Roth, Y. Kong, L. Xu, Z. Sartania, in *Proceedings of the Conference on Lasers and Electro Optics* (2008), paper CTuE3.

## Full References

- [1] V. Loriot, E. Hertz, O. Faucher, and B. Lavorel, “Measurement of high order Kerr refractive index of major air components”, *Optics Express* **17**, pp. 13429-13434 (2009); “Measurement of high order Kerr refractive index of major air components: erratum”, *Optics Express* **18**, pp. 3011–3012 (2010).
- [2] A. Couairon and A. Mysyrowicz, “Femtosecond filamentation in transparent media”, *Physics Reports* **441**, pp. 47-189 (2007).
- [3] L. Bergé, S. Skupin, R. Nuter, J. Kasparian, and J.-P. Wolf, “Ultrashort filaments of light in weakly ionized, optically transparent media”, *Reports on Progress in Physics* **70**, pp. 1633-1713 (2007).
- [4] S. L. Chin, *Femtosecond Laser Filamentation* (Springer, 2010).
- [5] P. Béjot, J. Kasparian, S. Henin, V. Loriot, T. Vieillard, E. Hertz, O. Faucher, B. Lavorel, and J.-P. Wolf, “Higher-Order Kerr Terms Allow Ionization-Free Filamentation in Gases”, *Physical Review Letters* **104**, 103903 (2010).
- [6] M. Aközbek, M. Scalora, C. Bowden, and S. L. Chin, “White-light continuum generation and filamentation during the propagation of ultra-short laser pulses in air”, *Optics Communications* **191**, pp. 353-362 (2001).
- [7] A. Couairon, “Dynamics of femtosecond filamentation from saturation of self-focusing laser pulses”, *Physical Review A* **68**, 015801 (2003).
- [8] A. Vincotte and L. Bergé, “ $\chi^{(5)}$  susceptibility stabilizes the propagation of ultrashort laser pulses in air”, *Physical Review A* **70**, 061802(R) (2004).
- [9] P. Béjot, E. Hertz, J. Kasparian, B. Lavorel, J.-P. Wolf, and O. Faucher, “Transition from Plasma-Driven to Kerr-Driven Laser Filamentation” *Physical Review Letters* **106**, 243902 (2011).
- [10] P. Polynkin, M. Kolesik, E. Wright, and J. Moloney, “Experimental Tests of the New Paradigm for Laser Filamentation in Gases”, *Physical Review Letters* **106**, 153902 (2011).
- [11] O. Kosareva, J.-F. Daigle, N. Panov, T. Wang, S. Hosseini, S. Yuan, G. Roy, V. Makarov, and S. L. Chin, “Arrest of self-focusing collapse in femtosecond air filaments: higher order Kerr or plasma defocusing?”, *Optics Letters* **36**, pp. 1035-1037 (2011).
- [12] Y.-H. Chen, S. Varma, T. Antonsen, and H. Milchberg, “Direct Measurement of the Electron Density of Extended Femtosecond Laser Pulse-Induced Filaments”, *Phys. Rev. Lett.* **105**, 215005 (2010).
- [13] A. Teleki, E. Wright, and M. Kolesik, “Microscopic model for the higher-order nonlinearity in optical filaments”, *Physical Review A* **82**, 065801 (2010).
- [14] C. Bree, A. Demircan, and G. Steinmeyer, “Saturation of the All-Optical Kerr Effect”, *Phys. Rev. Lett.* **106**, 183902 (2011).
- [15] J. Wahlstrand, Y.-H. Cheng, and H. Milchberg, “Optical nonlinearity in Ar and N<sub>2</sub> near the ionization threshold”, arXiv:1105.6334.v1.
- [16] M. Kolesik, E. Wright, and J. Moloney, “Femtosecond filamentation in air and higher-order nonlinearities”, *Optics Letters* **35**, pp. 2550-2552 (2010).
- [17] K. Kosma, S. Trushin, W. Schmid, and W. Fuss, “Vacuum ultraviolet pulses of 11 fs from fifth-harmonic generation of a Ti:Sapphire laser”, *Optics Letters*, **33**, pp. 723-725 (2008).
- [18] P. Béjot, E. Hertz, B. Lavorel, J. Kasparian, J.-P. Wolf, and O. Faucher, *Optics Letters*, “From higher-order Kerr nonlinearities to quantitative modeling of third and fifth harmonic generation in argon”, **36**, pp. 828-830 (2011).
- [19] P. Tzankov, M. Roth, Y. Kong, L. Xu, Z. Sartania, “Spatio-Temporal Characterization of the Signal Pulse-Shortening in Type II Optical Parametric Amplifier Using BBO and BIBO crystals”, in *Proceedings of the Conference on Lasers and Electro Optics* (2008), paper CTuE3.